Monthly Notices of the ROYAL ASTRONOMICAL SOCIETY

MNRAS **534,** 695–725 (2024) https://doi.org/10.1093/mnras/stae2102
Advance Access publication 2024 September 18

The *Gaia* ultracool dwarf sample–IV. GTC/OSIRIS optical spectra of *Gaia* late-M and L dwarfs

W. J. Cooper [1,2★] H. R. A. Jones,[1★] R. L. Smart,[2★] S. L. Folkes,[1] J. A. Caballero,[3] F. Marocco [4] M. C. Gálvez Ortiz,[3] A. J. Burgasser [5] J. D. Kirkpatrick,[4] L. M. Sarro,[6] B. Burningham [1] A. Cabrera-Lavers,[7] P. E. Tremblay,[8] C. Reylé,[9] N. Lodieu,[10,11] Z. H. Zhang [12,13] N. J. Cook,[14] J. F. Faherty,[15] D. García-Álvarez,[7,10] D. Montes [16] D. J. Pinfield,[1] A. S. Rajpurohit[17] and J. Shi[18,19]

[1]*Centre for Astrophysics Research, University of Hertfordshire, Hatfield, Hertfordshire AL10 9AB, UK*
[2]*Istituto Nazionale di Astrofisica, Osservatorio Astrofisico di Torino, Strada Osservatorio 20, I-10025 Pino Torinese, Italy*
[3]*Centro de Astrobiología (CAB), CSIC-INTA, Camino Bajo del Castillo s/n, Campus ESAC, Villanueva de la Cañada, E-28692 Madrid, Spain*
[4]*IPAC, Mail Code 100-22, Caltech, 1200 E. California Boulevard, Pasadena, CA 91125, USA*
[5]*Center for Astrophysics and Space Science, University of California San Diego, La Jolla, CA 92093, USA*
[6]*Departamento de Inteligencia Artificial, ETSI Informática, UNED, Juan del Rosal, E-16 28040 Madrid, Spain*
[7]*GRANTECAN, Cuesta de San José s/n, Breña Baja, E-38712 La Palma, Spain*
[8]*Department of Physics, University of Warwick, Coventry CV4 7AL, UK*
[9]*Institut UTINAM, CNRS UMR6213, Université de Bourgogne Franche-Comté, OSU THETA Franche-Comté-Bourgogne, Observatoire de Besançon, BP 1615, F-25010 Besançon Cedex, France*
[10]*Instituto de Astrofísica de Canarias, E-38205 La Laguna, Tenerife, Spain*
[11]*Departamento de Astrofísica, Universidad de La Laguna, E-38206 La Laguna, Tenerife, Spain*
[12]*School of Astronomy and Space Science, Nanjing University, 163 Xianlin Avenue, Nanjing 210023, China*
[13]*Key Laboratory of Modern Astronomy and Astrophysics, Nanjing University, Ministry of Education, Nanjing 210023, China*
[14]*Institute for Research on Exoplanets, Université de Montréal, Département de Physique, C.P. 6128 Succ. Centre-ville, Montréal, QC H3C 3J7, Canada*
[15]*Department of Astrophysics, American Museum of Natural History, Central Park West at 79th Street, NY 10024, USA*
[16]*Departamento de Física de la Tierra y Astrofísica and IPARCOS-UCM (Instituto de Física de Partículas y del Cosmos de la UCM), Facultad de Ciencias Físicas, Universidad Complutense de Madrid, E-28040 Madrid, Spain*
[17]*Astronomy and Astrophysics Division, Physical Research Laboratory, Navrangapura, Ahmedabad 380009, India*
[18]*College of Astronomy and Space Sciences, University of Chinese Academy of Sciences, Beijing 100049, China*
[19]*Key Laboratory of Optical Astronomy, National Astronomical Observatories, Chinese Academy of Sciences, Beijing 100012, China*

Accepted 2024 September 5. Received 2024 September 5; in original form 2023 July 7

ABSTRACT

As part of our comprehensive, ongoing characterization of the low-mass end of the main sequence in the Solar neighbourhood, we used the OSIRIS instrument at the 10.4 m Gran Telescopio Canarias to acquire low- and mid-resolution ($R\approx300$ and $R\approx2500$) optical spectroscopy of 53 late-M and L ultracool dwarfs. Most of these objects are known but poorly investigated and lacking complete kinematics. We measured spectral indices, determined spectral types (six of which are new) and inferred effective temperature and surface gravity from BT-Settl synthetic spectra fits for all objects. We were able to measure radial velocities via line centre fitting and cross correlation for 46 objects, 29 of which lacked previous radial velocity measurements. Using these radial velocities in combination with the latest *Gaia* DR3 data, we also calculated Galactocentric space velocities. From their kinematics, we identified two candidates outside of the thin disc and four in young stellar kinematic groups. Two further ultracool dwarfs are apparently young field objects: 2MASSW J1246467+402715 (L4β), which has a potential, weak lithium absorption line, and G 196–3B (L3β), which was already known as young due to its well-studied primary companion.

Key words: brown dwarfs – stars: kinematics and dynamics – stars: late-type – stars: low-mass.

1 INTRODUCTION

Ultracool dwarfs (UCDs) are objects with effective temperatures $T_{\rm eff} \lessapprox 2700$ K (spectral type $\gtrsim$ M7 V; Kirkpatrick et al. 1999) continuing on from the low-mass tail of the main sequence, that consist of spectral types late-M, L, T, and Y dwarfs. These UCDs consist of a combination of low-mass stars and brown dwarfs. Brown dwarfs are substellar objects incapable of hydrogen fusion and are defined by mass, between the deuterium minimum mass burning limit, ∼13 Jupiter masses (Saumon et al. 1996; Chabrier et al. 2000), and the hydrogen minimum mass burning limit, ∼72 Jupiter masses (Baraffe et al. 1997; Chabrier & Baraffe 1997). The majority of

★ E-mail: w.cooper@herts.ac.uk (WJC); h.r.a.jones@herts.ac.uk (HRAJ); richard.smart@inaf.it (RLS)

known UCDs are within the Solar neighbourhood (e.g. Smart et al. 2019; Kirkpatrick et al. 2021; Sarro et al. 2023) with typically dim apparent optical magnitudes (*GaiaG* $\gtrapprox$ 17 mag). The closest stars to the Sun have been catalogued throughout the history of astronomy. For example, the Catalogue of Nearby Stars (CNS) from Gliese (1957) has been updated with every all-sky photometric and astrometric survey, including the most recent release using *Gaia* DR3 data (CNS5; Golovin et al. 2023). This Solar neighbourhood has been further described in the 'The Solar Neighbourhood' series by the Research Consortium on Nearby Stars (RECONS[1]) team with publications from Henry, Kirkpatrick & Simons (1994) to Vrijmoet et al. (2022). Specifically, M dwarfs within 30 pc were covered in another series of articles from Delfosse et al. (1999) to Crifo et al. (2005). Volume limited samples such as the recent Gaia Collaboration (100 pc, 2021b), Kirkpatrick et al. (20 pc, 2021), and Reylé et al. (10 pc, 2021) works provide important constraints on the initial mass function (Salpeter 1955; Scalo 1986; Kroupa 2001; Chabrier 2003), which underpins all aspects of astrophysics from stars to galaxies to cosmology.

Spectral features of low mass stars, M, L, and T dwarfs, and their definitions were initially described by Tinney & Reid (1998), Kirkpatrick et al. (1999), Martín et al. (1999b), Burgasser et al. (2002), Geballe et al. (2002), and Kirkpatrick (2005). The bulk of the flux emitted by L dwarfs lies in the near infrared (NIR) and continues strongly towards the mid-infrared spectral regions for later spectral type UCDs. However, several features of youth, e.g. a weak sodium doublet, λλ8183,8195 Å (Schiavon et al. 1997a), are apparent in mid- to high-resolution optical spectra. Additionally, in the optical regime features such as the λ9850–10200 Å FeH Wing-Ford band (Schiavon, Barbuy & Singh 1997b) can be seen, which can be indicative of low or high metallicity. Optical spectra have an advantage in that there are fewer and weaker telluric absorption bands than in ground-based infrared spectra, where water and oxygen bands can dominate (Reiners et al. 2007; Smette et al. 2015). However, only the closest and brightest UCDs can be observed with optical spectroscopy due to the low relative flux; further and fainter UCDs require large aperture telescopes and long exposure times.

UCDs have typically been selected from photometric criteria using optical and near- to mid-infrared imaging surveys, supported by proper motion analysis. Examples of optical surveys include SuperCOSMOS (Hambly et al. 2001), *Gaia* (Gaia Collaboration 2016), Pan-STARRS (PS1; Chambers et al. 2016), and the SDSS (York et al. 2000; Abazajian et al. 2009), in which UCDs appear red. Notable infrared surveys and catalogues include 2MASS (Cutri et al. 2003; Skrutskie et al. 2006), DENIS (Epchtein et al. 1997), VISTA's VVV/VIRAC/VHS (Minniti et al. 2010; Smith et al. 2018; McMahon et al. 2021), and UKIDSS (Lawrence et al. 2007). Further infrared is the *WISE* (Wright et al. 2010) survey, which was expanded upon in the unWISE/catWISE (Schlafly, Meisner & Green 2019; Marocco et al. 2021; Meisner et al. 2023) catalogues. These NIR surveys are complemented by additional surveys constraining UCDs in open clusters such as the Pleiades (Steele & Jameson 1995; Pinfield et al. 2000; Lodieu, Deacon & Hambly 2012), or elsewhere (Lucas & Roche 2000; Zapatero Osorio et al. 2000; Burningham et al. 2013).

The photometry of UCDs is important because the change in colour across the optical and NIR regime (Leggett et al. 2002) correlates with physical and atmospheric properties. These changing processes, such as dust, condensate cloud formation, and subsequent clearing as an atmosphere cools, are well covered in the literature (e.g. Dahn et al. 2002; Marley et al. 2002; Saumon & Marley 2008). Understanding a changing atmosphere for different ages with a range of masses has allowed the computing of 'cooling tracks' (Burrows et al. 1997; Baraffe et al. 2015). Accounting for theoretical atmospheric physics has been used in model grids such as BT-Settl (Allard, Homeier & Freytag 2011), or Sonora (Karalidi et al. 2021; Marley et al. 2021), and when interpreting the results of retrieval techniques (e.g. Burningham et al. 2017; Calamari et al. 2022). Being able to constrain the mass and/or age has underpinned modern observational UCD astronomy, but is challenging due to the mass/age degeneracy (Burrows et al. 1997). For example, benchmark systems (e.g. Pinfield et al. 2006; Dupuy, Liu & Ireland 2009) allow us to constrain the age of a brown dwarf with the coeval main sequence primary. The metallicity and surface gravity of an object of a given spectral type are the major variables affecting the photometric colour (Stephens et al. 2009), see references to 'blue' and 'red' L dwarfs (e.g. Faherty et al. 2009; Schmidt et al. 2010). Any works that infer spectral type, surface gravity, and effective temperature must take into account the atmospheric physics, as these directly correlate with observable features.

Gaia is a European Space Agency mission, launched in 2013 to make high-precision measurements of positions, parallaxes, and proper motions of well over a billion sources and photometry in three different photometric filters (G_{BP}, G, G_{RP}). The third *Gaia* data release (EDR3 and DR3–Gaia Collaboration 2021a, 2023, respectively) containing astrometric and photometric measurements, was in 2021 December, with the remaining measurements and inferred parameters, including spectra, in 2022 June.[2]

Obtaining the full 6D (right ascension, declination, proper motions, parallax, radial velocity: α, δ, $\mu_\alpha \cos\delta$, μ_δ, ϖ, v_r) positional and kinematic information is fundamental to fully characterize the populations of UCDs within a volume-limited sample (e.g. Best et al. 2021). Precise measurements of radial velocities (RVs) are obtained from high signal-to-noise observations taken with high resolution spectrographs with resolving powers of $R\sim$100 000, leading to uncertainties $\sim$1–5 m s^{-1}. This has only been achievable for the nearest, brightest UCDs (e.g. Zechmeister et al. 2019). Blake, Charbonneau & White (2010) achieved $\delta v_r \approx$ 50–200 m s^{-1} with the Keck Near-Infrared Spectrometer (NIRSPEC), which had a resolution of $R\approx$25 000. The 'Brown Dwarf Kinematics Project' has gathered further UCD RVs (Burgasser et al. 2015; Hsu et al. 2021) with both the NIRSPEC and the Magellan Echellette (MagE, $R\sim$4100, $\delta v_r \approx$ 2–3 km s^{-1}) spectrographs. By comparison, the lower resolution spectroscopy such as those discussed in this work ($R\approx$2500) is only capable of theoretical minimum uncertainties of $\gtrsim$5 km s^{-1}; this is still useful when constraining the kinematics of the Solar neighbourhood. Parallaxes and proper motions of UCDs were historically gathered from ground based time-domain campaigns (e.g. PARSEC: Andrei et al. 2011; Marocco et al. 2013; Smart et al. 2018) that have been generally superseded by *Gaia* for the brightest objects, $G \lessapprox$ 20 mag. In the case of most late-L and T dwarfs, ground-based astrometry is still the predominant source (e.g. Vrba et al. 2004; Dupuy & Liu 2012; Liu, Dupuy & Allers 2016; Best et al. 2018). For dimmer objects, beyond mid-L dwarfs, parallaxes and proper motions are gathered by space-based infrared surveys and are analysed in-depth by Kirkpatrick et al. (2021). Young moving groups are constrained using these complete kinematics. See

[1] http://www.astro.gsu.edu/RECONS/

[2] The astrometry and photometry in *Gaia* DR3 used in this work is identical to that within *Gaia* EDR3 whilst the astrophysical parameters are purely from *Gaia* DR3; hence, both data releases are cited here.

Table 1. The 53 targets observed at the GTC with OSIRIS and presented in this work.

Object short name	*Gaia* DR3 source ID	α [hms]	δ [dms]	ϖ [mas]	G [mag]	J [mag]	Grism/VPHG
J0028−1927	2 363 496 283 669 200 768	0 28 55.6	−19 27 16	25.742	18.97	14.19	R2500I
J0235−0849	5 176 990 610 359 832 576	2 35 47.5	−8 49 20	21.742	20.35	15.57	R2500I
J0428−2253	4 898 159 654 173 165 824	4 28 51.1	−22 53 20	39.398	18.72	13.51	R2500I
J0453−1751	2 979 566 285 233 332 608	4 53 26.5	−17 51 55	33.064	20.14	15.14	R2500I
J0502+1442	3 392 546 632 197 477 248	5 02 13.5	+ 14 42 36	21.746	18.90	14.27	R2500I
J0605−2342	2 913 249 451 860 183 168	6 05 01.9	−23 42 25	30.185	19.31	14.51	R2500I
J0741+2316	867 083 081 644 418 688	7 41 04.4	+ 23 16 38	13.019	20.83	16.16	R2500I
J0752+4136	920 980 385 721 808 128	7 52 59.4	+ 41 36 47	11.734	17.71	14.00	R2500I
J0809+2315	...	8 09 10.7[1]	+ 23 15 16[1]	...	...	16.72	R2500I
J0823+0240	3 090 298 891 542 276 352	8 23 03.1	+ 2 40 43	...	21.18	16.06	R2500I
J0823+6125	1 089 980 859 123 284 864	8 23 07.3	+ 61 25 17	39.467	19.66	14.82	R2500I
J0847−1532	5 733 429 157 137 237 760	8 47 28.9	−15 32 41	57.511	18.38	13.51	R300R
J0918+2134	...	9 18 38.2[2]	+ 21 34 06[2]	...	...	15.66	R2500I
J0935−2934	5 632 725 432 610 141 568	9 35 28.0	−29 34 58	29.969	19.00	14.04	R2500I
J0938+0443	3 851 468 354 540 078 208	9 38 58.9	+ 4 43 43	15.448	19.89	15.24	R2500I
J0940+2946	696 581 955 256 736 896	9 40 47.7	+ 29 46 52	17.961	20.30	15.29	R2500I
J0953−1014	3 769 934 860 057 100 672	9 53 21.2	−10 14 22	28.022	18.44	13.47	R2500I
J1004+5022	824 017 070 904 063 488	10 04 20.4	+ 50 22 56	46.195	20.13	14.83	R300R & R2500I
J1004−1318	3 765 325 471 089 276 288	10 04 40.2	−13 18 22	40.438	19.84	14.68	R2500I
J1047−1815	3 555 963 059 703 156 224	10 47 30.7	−18 15 57	35.589	19.01	14.20	R300R & R2500I
J1058−1548	3 562 717 226 488 303 360	10 58 47.5	−15 48 17	55.098	19.24	14.16	R300R & R2500I
J1109−1606	3 559 504 797 109 475 328	11 09 26.9	−16 06 56	24.161	19.65	14.97	R2500I
J1127+4705	785 733 068 161 334 656	11 27 06.5	+ 47 05 48	23.758	19.94	15.20	R2500I
J1213−0432	3 597 096 309 389 074 816	12 13 02.9	−4 32 44	59.095	19.86	14.68	R2500I
J1216+4927	1 547 294 197 819 487 744	12 16 45.5	+ 49 27 45	...	20.92	15.59	R2500I
J1221+0257	3 701 479 918 946 381 184	12 21 27.6	+ 2 57 19	53.812	17.86	13.17	R2500I
J1222+1407	...	12 22 59.3[3]	+ 14 07 50[3]	...	...	...	R300R
J1232−0951	3 579 412 039 247 581 824	12 32 18.1	−9 51 52	34.5[4]	18.74	13.73	R2500I
J1246+4027	1 521 895 105 554 830 720	12 46 47.0	+ 40 27 13	44.738	20.28	15.09	R300R & R2500I
J1331+3407	1 470 080 890 679 613 696	13 31 32.6	+ 34 07 55	34.791	19.01	14.33	R300R & R2500I
J1333−0215	3 637 567 472 687 103 616	13 33 45.1	−2 16 02	26.599	20.10	15.38	R2500I
J1346+0842	3 725 064 104 059 179 904	13 46 07.2	+ 8 42 33	23.339	20.47	15.74	R2500I
J1412+1633	1 233 008 320 961 367 296	14 12 24.5	+ 16 33 10	31.278	18.67	13.89	R300R & R2500I
J1421+1827	1 239 625 559 894 563 968	14 21 30.6	+ 18 27 38	52.862	17.84	13.23	R2500I
J1439+0039	...	14 39 15.1[1]	+ 0 39 42[1]	...	...	18.00	R300R
J1441−0945	6 326 753 222 355 787 648	14 41 36.9	−9 46 00	32.505	19.22	14.02	R300R & R2500I
J1527+0553	...	15 27 22.5[1]	+ 5 53 16[1]	...	...	17.63	R300R
J1532+2611	1 222 514 886 931 289 088	15 32 23.3	+ 26 11 19	...	21.08	16.12	R2500I
J1539−0520	4 400 638 923 299 410 048	15 39 42.6	−5 20 41	59.266	18.98	13.92	R2500I
J1548−1636	6 260 966 349 293 260 928	15 48 58.1	−16 36 04	37.535	18.54	13.89	R2500I
J1617+7733B	1 704 566 318 127 301 120	16 17 06.5	+ 77 34 03	13.705	16.55	13.10	R300R & R2500I
J1618−1321	4 329 787 042 547 326 592	16 18 44.9	−13 21 31	21.86[5]	19.34	14.25	R2500I
J1623+1530	4 464 934 407 627 884 800	16 23 21.8	+ 15 30 39	10.301	20.59	15.94	R2500I
J1623+2908	...	16 23 07.4[2]	+ 29 08 28[2]	...	...	16.08	R2500I
J1705−0516	4 364 462 551 205 872 000	17 05 48.5	−5 16 48	53.122	18.19	13.31	R300R
J1707−0138	4 367 890 618 008 483 968	17 07 25.3	−1 38 10	25.976	19.25	14.29	R300R & R2500I
J1717+6526	1 633 752 714 121 739 264	17 17 14.5	+ 65 26 20	45.743	20.26	14.95	R300R & R2500I
J1724+2336	4 569 300 467 950 928 768	17 24 37.4	+ 23 36 50	14.625	20.19	15.68	R300R
J1733−1654	4 124 397 553 254 685 440	17 33 42.4	−16 54 51	54.935	18.50	13.53	R300R
J1745−1640	4 123 874 907 297 370 240	17 45 34.8	−16 40 56	50.918	18.44	13.65	R2500I
J1750−0016	4 371 611 781 971 072 768	17 50 24.4	−0 16 12	108.581	18.29	13.29	R2500I
J2155+2345	1 795 137 592 033 253 888	21 55 58.6	+ 23 45 30	...	20.93	15.99	R2500I
J2339+3507	2 873 220 249 284 763 392	23 39 25.5	+ 35 07 16	36.230	20.46	15.36	R2500I

Note. References – Positions all at 2016.5 except at the indicated epochs:
1. Lawrence et al. (2007) – 2008,
2. Skrutskie et al. (2006) – 1998–2000,
3. Chambers et al. (2016) – 2012–2013,
4. Best et al. (2020) – 2014–2018,
5. Weinberger et al. (2016) – 2007–2013.

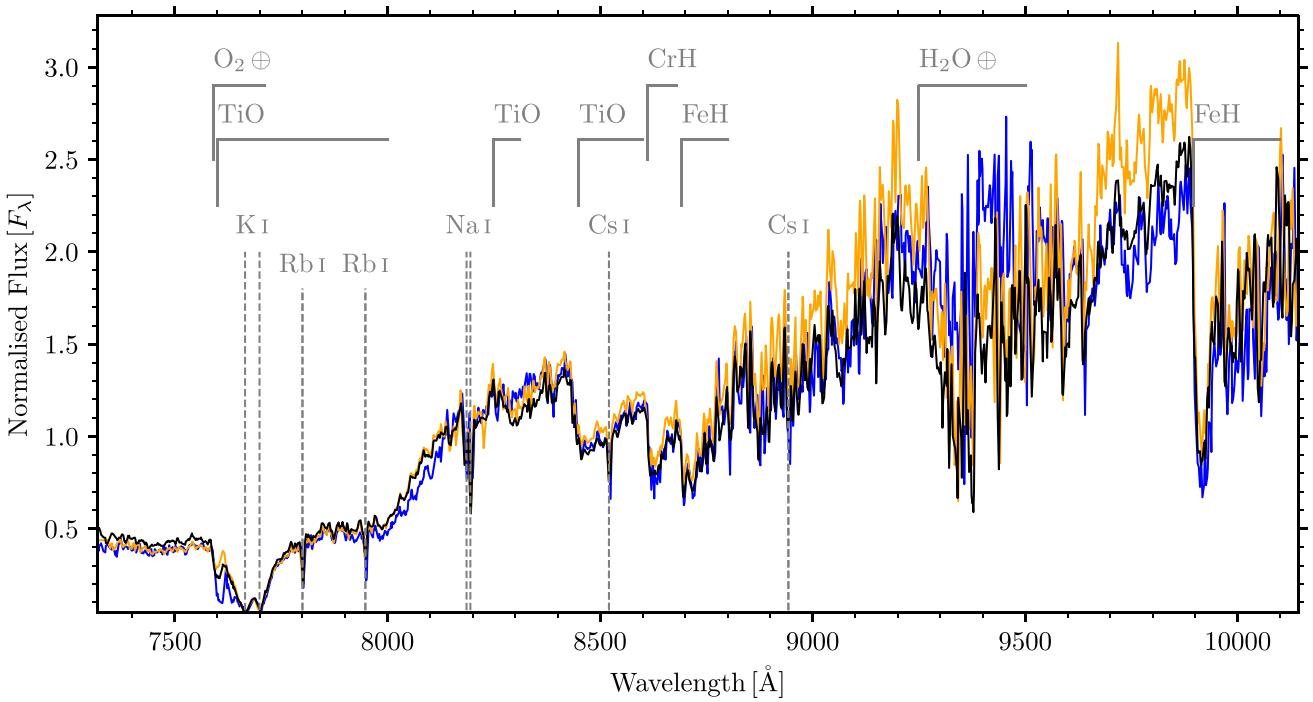

Figure 1. R2500I spectra for J1745−1640, normalized at 8100–8200 Å, comparing two independent reduction procedures: `PYPEIT` in black and `IRAF` in orange. In blue, the heliocentric corrected MagE spectra (Burgasser et al. 2015) for the same object is shown (which is not telluric corrected). The Earth symbol indicates the telluric bands present in the spectra.

the BANYAN Σ series and references therein for detail on nearby young moving groups and clusters (Gagné et al. 2014, to Gagné & Faherty 2018) or similarly, the LACEwING code (Riedel et al. 2017), designed around young objects in the Solar neighbourhood. Subdwarfs, meanwhile, are characterized by their statistically higher space velocities indicative of the older population (e.g. Lodieu et al. 2005; Burgasser, Cruz & Kirkpatrick 2007; Lodieu et al. 2017; Zhang et al. 2017).

This is the fourth item in the *Gaia* UltraCool Dwarf Sample series (GUCDS; Smart et al. 2017, 2019; Marocco et al. 2020) and is an ongoing, international, multiyear programme aimed at characterizing all of the UCDs visible to *Gaia*.*Gaia* DR3 produced astrophysical parameters for ≈470 million sources (Creevey et al. 2023), including effective temperatures, $T_{\rm eff}$. The ≈94 000 *Gaia* DR3 $T_{\rm eff}$ values relating to UCDs by Creevey et al. (2023) were provided under the `teff_espucd` keyword. The full sample of UCDs detected by *Gaia* with *Gaia* DR3 $T_{\rm eff}$ values were documented and analysed by Sarro et al. (2023). In our analysis, we will use the values from these *Gaia* DR3 derivative works to compare with the equivalent values directly measured by us. There is significant overlap between the Sarro et al. (2023) sample and the GUCDS, although the majority of UCD sources as seen by *Gaia* are as yet not characterized through spectroscopic follow-up. A subset of this Sarro et al. (2023) sample has public *Gaia* RP spectra (see the *Gaia*xp_summary table[3]), which covers the $G_{\rm RP}$ passband ($\Delta\lambda \approx$ 6200–10420 Å; Riello et al. 2021). This subset from Sarro et al. (2023) was further analysed for spectroscopic outliers by Cooper et al. (2024). The internally calibrated *Gaia* RP spectra and processing were discussed thoroughly by Carrasco et al. (2021), De Angeli et al. (2023), and Montegriffo et al. (2023).

The aim of this work is to complement the literature population with measurements and inferences from low- and mid-resolution optical spectroscopy. In Section 2.2 we explain the target selection (Section 2.1) and observation strategy (Section 2.2). Different reduction techniques with a test case are discussed in Section 3. Section 4 explains our techniques for determining spectral types (Section 4.1), astrophysical parameters (Section 4.2), and kinematics (Section 4.3) including membership in moving groups (Section 4.4). Section 5 follows a discussion of our results for spectral types (Section 5.1), kinematics (Section 5.2), and astrophysical parameters (Section 5.3). We also discuss individual objects (Section 5.3.1) before summarizing the overall conclusions in Section 6.

2 DATA COLLECTION

We obtained optical spectroscopy of 53 unique UCDs using the OSIRIS (Optical System for Imaging and low-intermediate Resolution Integrated Spectroscopy–Cepa 1998) instrument on the 10.4 m Gran Telescopio Canarias (GTC) at El Roque de los Muchachos in the island of La Palma, Spain, under proposal IDs GTC54-15A and GTC8-15ITP (PIs Caballero and Marocco, respectively). The objects were observed in semesters 2015A, 2015B, and 2016A.

The observed data from the GTC were complemented with *Gaia* DR3. *Gaia* also carries a radial velocity spectrometer, although this was unsuitable for our purposes as all of our targets were fainter than the *Gaia* selection limit (Katz et al. 2023; $G < 14$ mag,).

We acquired 63 spectra in which we observed 53 unique objects, shown in Table 1. These 63 observations are shown in Table A1,

[3]https://gea.esac.esa.int/archive/documentation/GDR3/Gaia_archive/chap_datamodel/sec_dm_spectroscopic_tables/ssec_dm_xp_summary.html

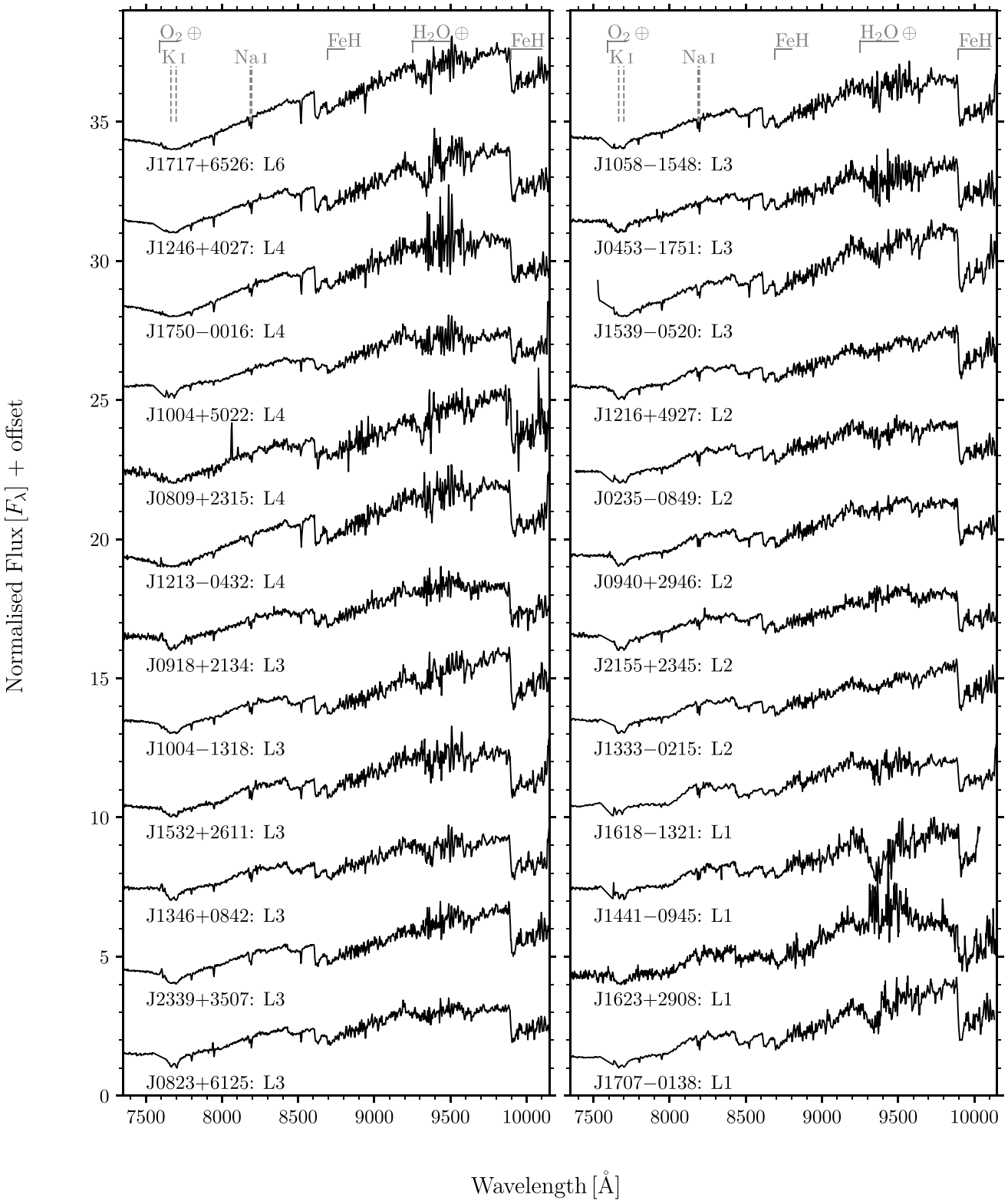

Figure 2. The first 24 of the R2500I VPHG spectra with a linear offset applied, sorted by spectral subtype. We show the short names and the spectral subtypes from this work, attached to each spectrum. At the top of the figure are grey lines denoting a selection of spectral features typical to L dwarfs, plus the two main telluric bands.

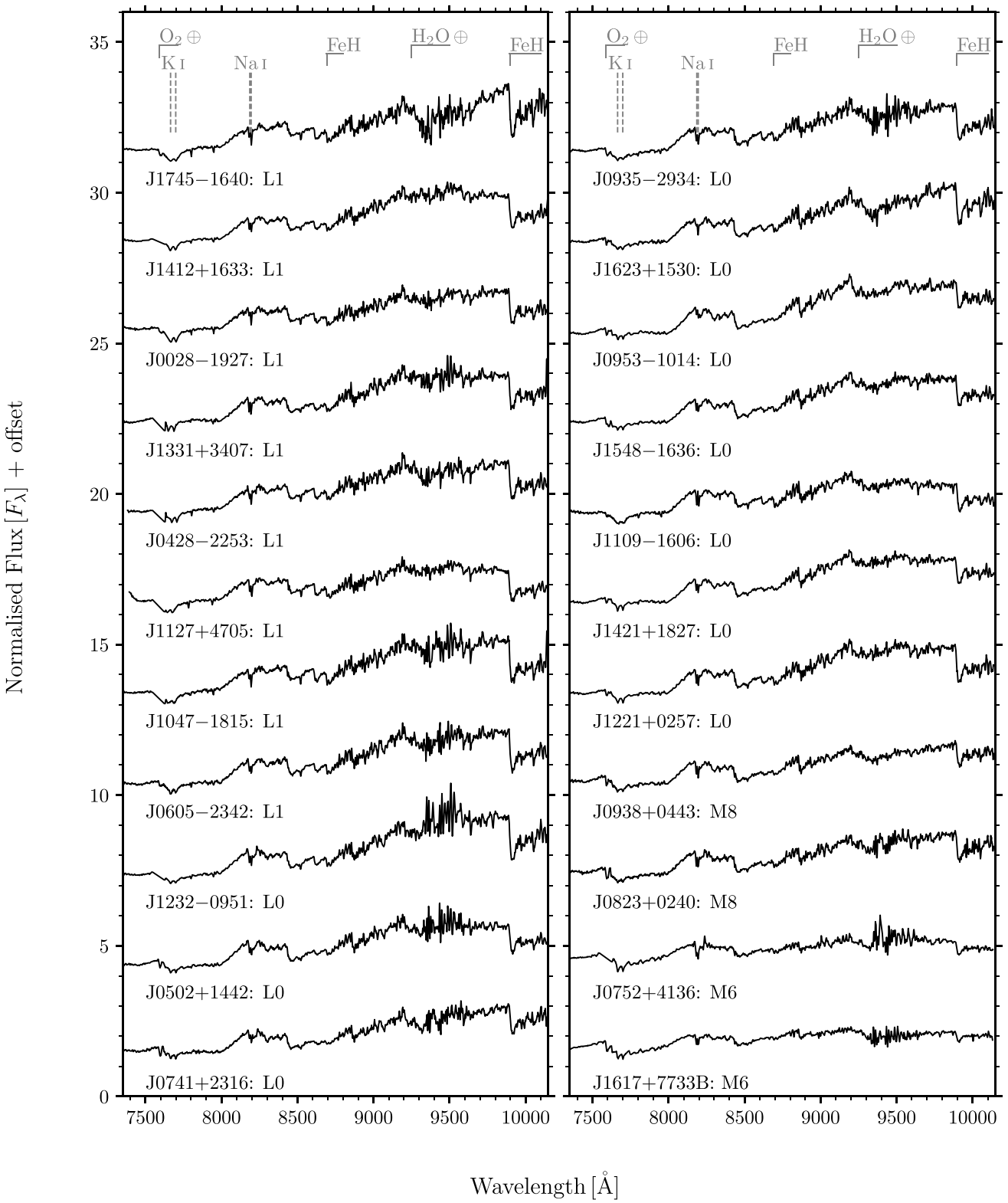

Figure 3. Same as Fig. 2 but for the second half of the R2500I VPHG sample.

including the airmass and humidity of the observation. Of the 63 spectra, 46 were observed with the R2500I volume phased holographic grating (hereafter VPHG), whilst 17 were observed with the R300R grism. Ten of the 53 objects were observed with both dispersive elements.

Twenty of the 53 objects already had full 6D positional and kinematic information in the literature. Fifty-one had proper motions, 43 had parallaxes, and two had only α and δ. All values along with their provenance are given in Table 1. In the next subsections we discuss the target list selection and observations.

2.1 Target selection

Our targets were drawn from a combination of two samples: benchmark systems (system with a star and a UCD; Pinfield et al. 2006) and known L dwarfs with poor or no available spectroscopy. The targets were selected by Marocco et al. (2017, 2020), and here we briefly summarize their selection criteria. Both samples were chosen with the aim of gathering low- and mid-resolution spectra, mostly to achieve radial velocities and to confirm their status as L dwarfs. Benchmark system selection used the procedure of Marocco et al. (2017, their section 4). To summarize, primary systems consisting of possibly metal-rich or metal-poor stars were selected with metallicity cuts of [Fe/H] < -0.3 and [Fe/H] > 0.2 dex from a number of catalogues (Marocco et al. 2017, their table 2). If more than one value of [Fe/H] was available, the one with the smallest uncertainty was used; Marocco et al. (2017) did not investigate if there were any systematic offsets between different catalogues, as this was beyond the scope of that work. The companions to these systems were filtered by a series of colour, absolute magnitude, and photometric quality cuts from 2MASS, SDSS (the Sloan Digital Sky Survey; York et al. 2000) and ULAS (United Kingdom Infrared Telescope Deep Sky Survey, Large Area Survey; Lawrence et al. 2007) photometry in equation (1). These colour cuts in equation (1) are taken directly from Marocco et al. (2017) as that work created part of the target list used in this work. Magnitudes from 2MASS were converted into UKIRT/WFCAM magnitudes via the equations of Stephens & Leggett (2004).

$$
\begin{aligned}
&Y - J > 0.85;\\
&J - H > 0.50;\\
&z - J > 2.1;\\
&\sigma_J < 0.1;\\
&[2.5 \times (z - J) + 4] < M_J < [5 \times (z - J) + 1];\\
&M_J > 11.5;\\
&1.6 < i - z < 6.0;\\
&11.5 < M_z < [3.5714 \times (i - z) + 9.286];\\
&M_z \geq 15;\\
&M_z \geq [3.5714 \times (i - z) + 6.5];\\
&i - z \leq 2.1. \qquad (1)
\end{aligned}
$$

These companions were determined as being candidate benchmark systems with a maximum matching radius of 3 arcmin, i.e. the maximum separation to the primary object. The remaining targets, known L dwarfs, were already spectroscopically confirmed bright L dwarfs that were predicted to be visible to the astrometry and photometry in (at the time, upcoming) *Gaia* data releases. These known L dwarfs should be single systems. They would, however, not be bright enough for the *Gaia* radial velocity spectrometer (Katz et al. 2023), and thus were chosen to determine radial velocities for, as a complement to the 30 pc volume-limited sample. This list was complemented with additional targets too dim for *Gaia* photometry and astrometry, which were detected in UKIDSS, and by a few well-known L dwarfs, such as G 196–3B, which could serve as template standards.

2.1.1 *Cross-matching*

All observed targets (Table 1) were cross-matched with *Gaia*, 2MASS, and AllWISE. These surveys were chosen because they are all-sky and we were aiming for completeness in this process. The targets were also cross-matched with Pan-STARRS (50/53 successful matches), for the additional optical components for those sources within the Pan-STARRS footprint. This sample of 53 objects was then also cross-matched against the astrophysical parameter and `xp_summary` tables from *Gaia* DR3.[4] Thirty-eight of these objects had a `teff_espucd` value, and 28 had a public RP spectrum. Internally calibrated *Gaia* RP spectra were then extracted from the *Gaia* archive with a linearly dispersed grid from 6000 Å to 10 500 Å using the `GAIAXPY.CONVERT` (Ruz-Mieres 2022) and `GAIAXPY-BATCH` (Cooper 2022a) codes. We also searched for common proper motion systems within Simbad (Wenger et al. 2000) with the selection criteria given in the GUCDS, specifically equation (1) of Marocco et al. (2020):

$$
\begin{aligned}
&\rho < 100\varpi;\\
&\Delta\varpi < \max[3\sigma_\varpi, 1];\\
&\Delta\mu < 0.1\mu;\\
&\Delta\theta < 15 \text{ deg}. \qquad (2)
\end{aligned}
$$

In equation (2), ρ is the separation in arcseconds, θ is the proper motion position angle in degrees, whilst ϖ (milli-arcseconds) and μ (milli-arcseconds per year) are our target list's *Gaia* DR3 parallax and proper motion, respectively. Like with the photometric selection, equation (1), the common proper motion selection was taken directly from Marocco et al. (2020). This is because the target list in this work is drawn from the same wider target list used in the GUCDS. In effect, this selection is creating a widest possible physical separation of 100 000 AU (see the discussion on binding energies by Caballero 2009).

2.2 Observations

The OSIRIS instrument used a 2×1 mosaic of 2048×4096 pixel (photosensitive area) red-optimized CCDs (Marconi MAT-44-82 type) with a 7.8×7.8 arcmin^2 unvignetted field of view. We used the standard operational mode of 2×2 binning, which has a physical pixel size of 0.254 arcsec pixel^{-1}. For our purposes, we used the 7.4 arcmin long slit with a width of 1.2 arcsec. We had variable seeing between 0.6 and 2.5 arcsec, with the vast majority having seeing <1.2–1.5. The undersampling of the full width at half-maximum (FWHM) when the seeing is significantly less than the slit width would cause uncertainty in the wavelength calibration. In the worst cases, this can approach the resolution element. This was then included in the systematic uncertainty estimate on the radial velocities. We used the R300R and R2500I grisms and purely read off CCD 2 due to the instrument calibration module having a strong gradient from CCD 1 to 2 in the flat fields. The

[4]These tables are logically distinct from the main *Gaia* table in terms of schema and completeness.

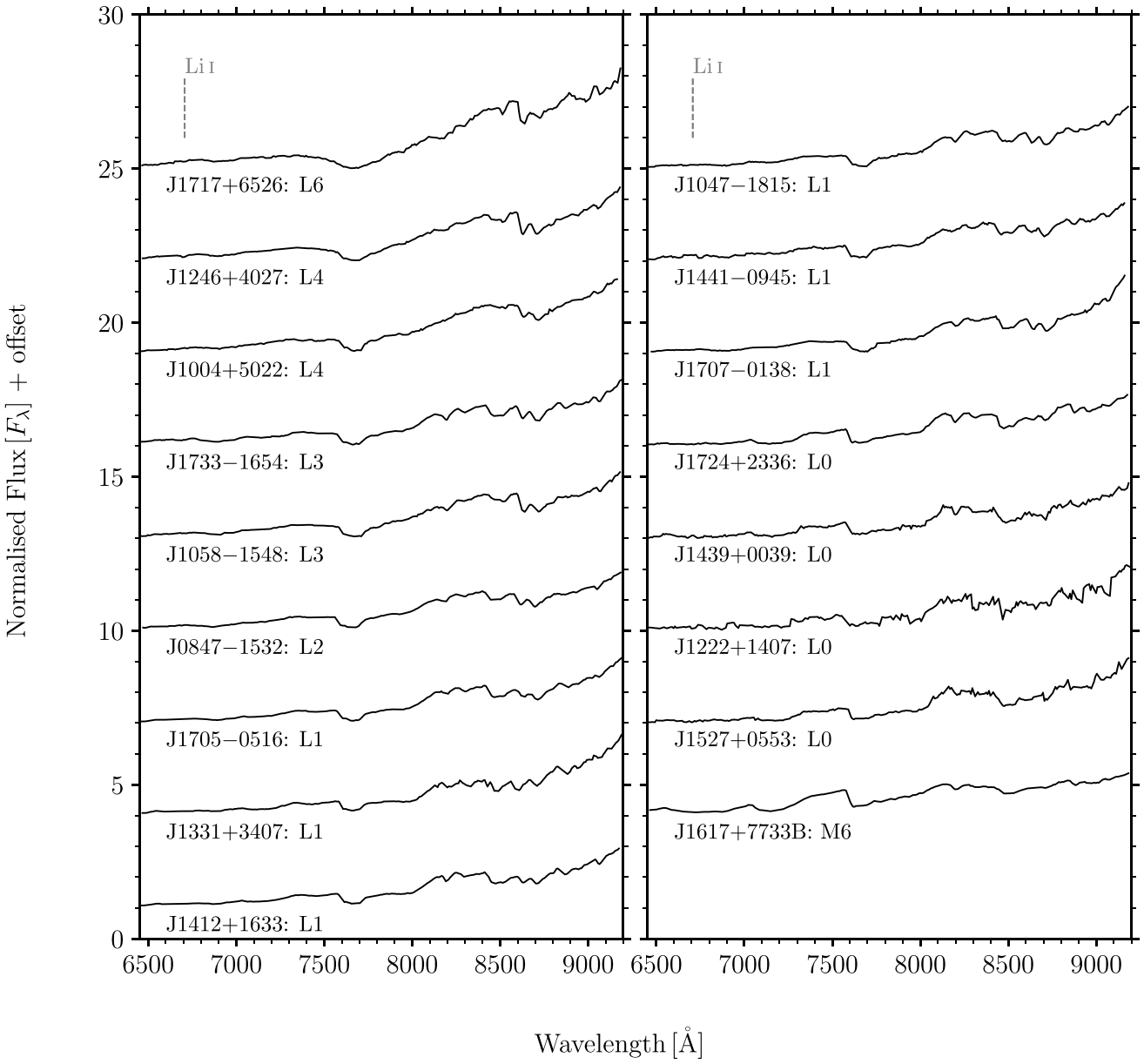

Figure 4. Same as Fig. 2 but for the R300R grism spectra. Instead of the spectral features visible in Figs 2 and 3, we only show where any lithium detection would be.

Table 2. The list of atomic alkali metal lines used when estimating astrophysical parameters and calculating radial velocities. Wavelengths are as measured by Kramida et al. (2021) and are defined in standard air.

Line	λ (Å)
K I-a	7664.8991
K I-b	7698.9646
Rb I-a	7800.268
Rb I-b	7947.603
Na I-a	8183.2556
Na I-b	8194.824
Cs I-a	8521.13165
Cs I-b	8943.47424

R300R grism has a wavelength range of ≈4800–10 000 Å with a dispersion of ≈7.74 Å pix^{-1} for a resolution of ≈350 whilst the R2500I VPHG has a wavelength range of ≈7330–10 000 Å with a dispersion of ≈1.36 Å pix^{-1} for a resolution of ≈2500, as per the online documentation.[5] Both dispersive elements experience an increase in fringing at wavelengths $\gtrsim$9200 Å to ≥5 per cent. The R300R grism however, had second-order light from 4800 to 4900 Å contaminating the 9600 to 9800 Å region. This is because standards, but not UCDs, have flux in the blue regime, hence affecting the flux calibration in the red regime. As a result, the R300R spectra were conservatively truncated to 9000 Å. Our standards were a selection of

[5] http://www.gtc.iac.es/instruments/osiris/osiris.php##Longslit_Spectroscopy

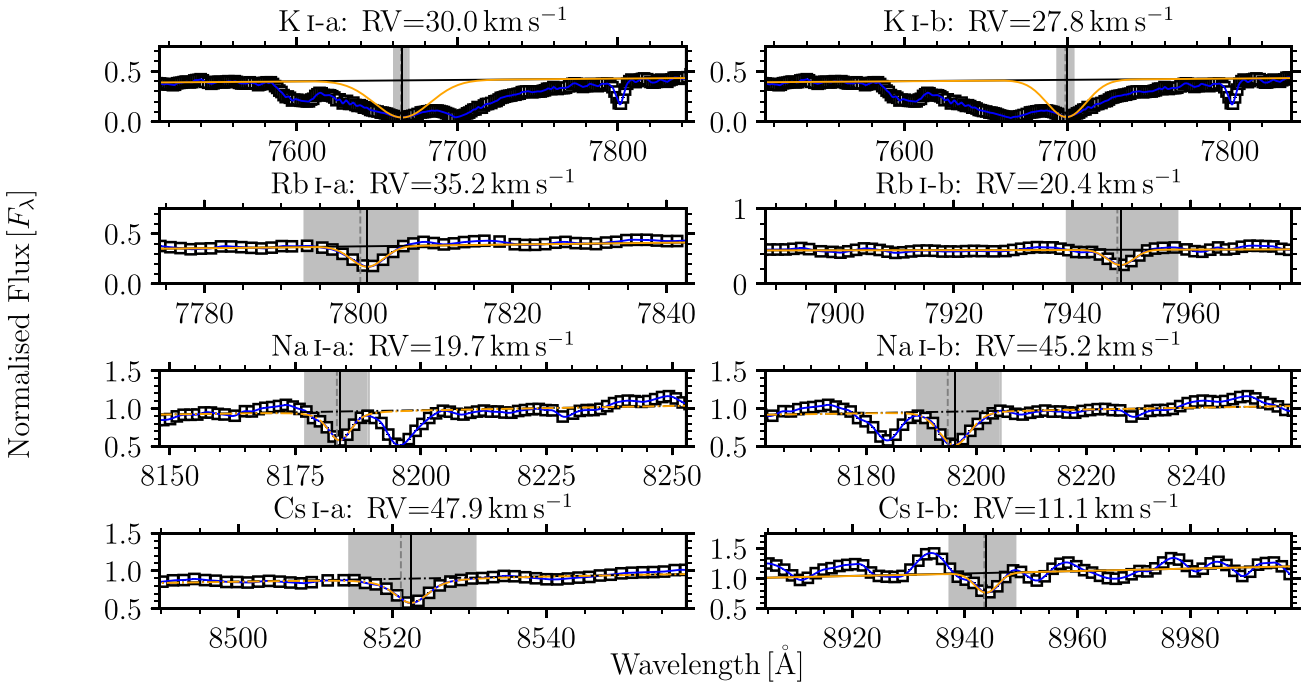

Figure 5. J1745−1640 RV calculation via different line profiles (orange: solid – Gaussian; dash-dot – Voigt) against the data (black squares) and fifth order spline fit (blue) in the regime around the eight listed line centres. The flux uncertainty is smaller than the height of each square. The shift from the laboratory line position (vertical dashed grey line) is shown as the vertical solid black line. The horizontal black line (solid or dash-dot, depending on the fitted line profile as above) is the continuum, as is subtracted from the data. A grey band is given, corresponding to the region of data the line profiles are fitted to. The shown region is between the inner edges of the continuum regions.

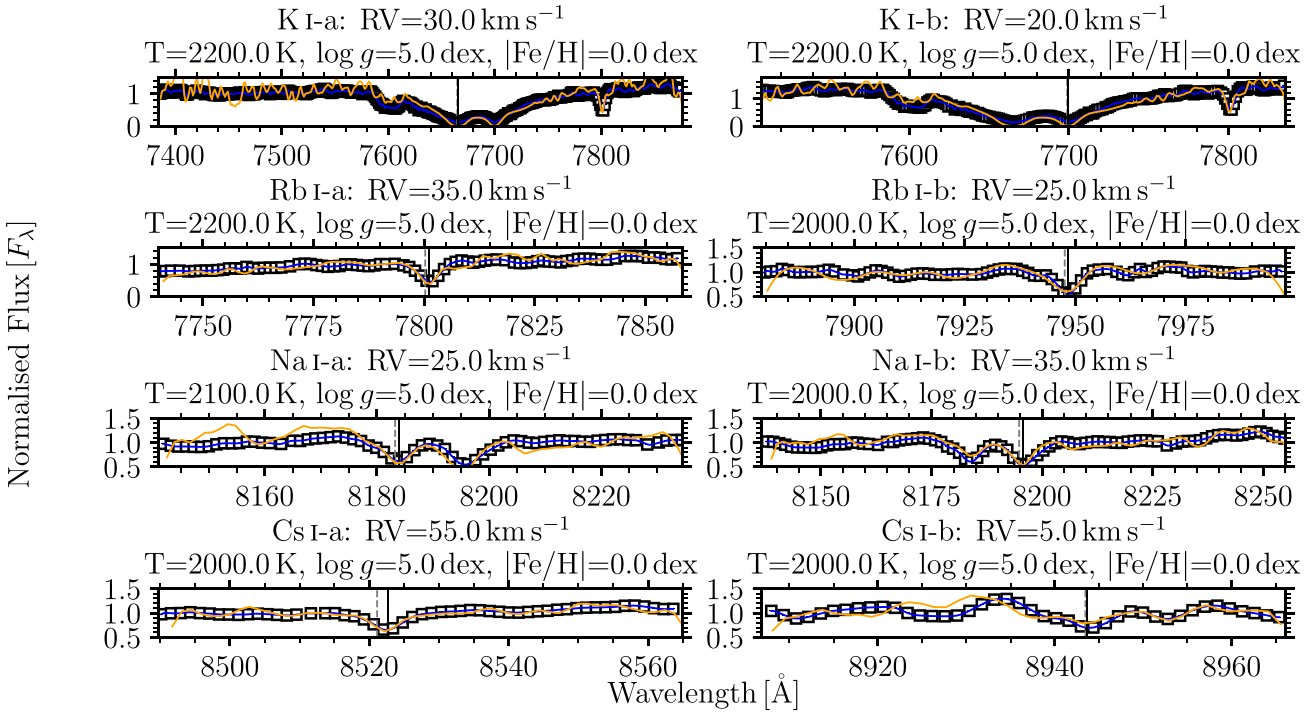

Figure 6. J1745−1640 RV calculation via the manually shifted BT-Settl model (orange) against the data (black squares) and fifth-order spline fit (blue). The flux uncertainty is smaller than the height of each square. The laboratory line position (vertical dashed grey line) has been manually shifted by the RV given on the sub-plot title (vertical solid black line). Effective temperature, gravity, and metallicity are also indicated on each features title.

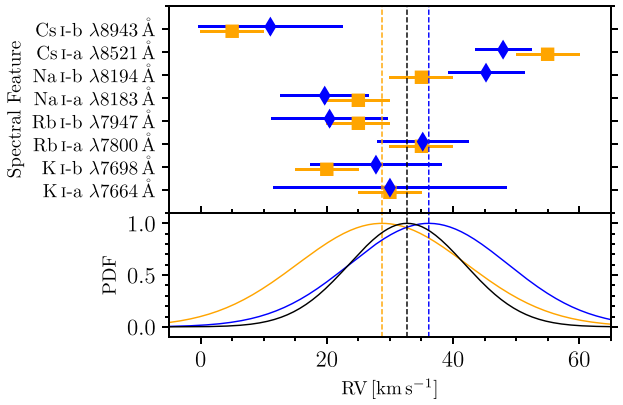

Figure 7. J1745−1640 RV values for each given line. In the top panel, orange squares are cross-correlated RVs, blue diamonds are line centre RVs; each spectral feature has been indicated on the y axis. In the bottom panel, the orange curve is the cross-correlated PDF; the blue curve is the line centre PDF; and the black curve is the adopted PDF. The dotted vertical lines are the mean RV values as associated with each PDF.

white dwarfs plus two well-studied bright main sequence dwarf stars, all with literature flux calibrated spectra and spectral types: Ross 640 (DZA6; Oke 1974; McCleery et al. 2020); Hilt 600 (B1; Hamuy et al. 1992, 1994); GD 153 (DA1; Bohlin, Colina & Finley 1995; Bohlin, Gordon & Tremblay 2014); G191-B2B (DA1; Oke 1990; Bohlin et al. 1995; Bohlin et al. 2014); GD 248 (DC5; Tremblay, Bergeron & Gianninas 2011; McCleery et al. 2020), GD 140 (DA2; Tremblay et al. 2011; McCleery et al. 2020), and G 158-100 (dG-K; Oke 1990). We took a series of short exposures for the brightest objects to avoid saturation and non-linearity. The majority of observations had a bright moon whilst the sky condition varied from photometric to clear with humidity typically $\lesssim$50 per cent. All calibration frames were taken at the start and end of each night, the arc lamps being used to solve the wavelength solution were: Hg-Ar, Ne, and Xe. The full observing log is given in Table A1.

3 DATA REDUCTION

We aimed to determine spectral types, spectral indices, and radial velocities from directly measuring the GTC spectra. Furthermore, we inferred astrophysical parameters (effective temperature, $T_{\rm eff}$ (K); surface gravity, log g (dex); and metallicity, [Fe/H] [dex]) from comparisons with atmospheric models.

Our adopted PypeIt[6] (Prochaska et al. 2020a, b) reduction procedure applied to every object was as follows: master calibration files were created by median stacking the relevant flat, bias, and arc frames. Basic image processing was performed including bias subtraction, flat fielding, spatial flexure correction, and cosmic ray masking via the L.A. Cosmic Rejection algorithm (van Dokkum 2001). We then manually identified the arc lines using the median stacked master arc. These arc lines were used to manually create a wavelength solution through `PYPEIT_IDENTIFY` with typical RMS values of ≈0.0804 Å for the R2500I VPHG and ≈0.1394 Å for the R300R grism. The R2500I wavelength calibration solution was a sixth-order polynomial, whilst the R300R solution was only third. The information inside the object headers (observation date, object sky position, longitude, and latitude of the observatory) was used to heliocentric correct the wavelength solution. The `PYPEIT` wavelength solution was defined in vacuum.

The standard frames were median stacked before the global sky was subtracted and corrected for spectral flexure (to account for fringing). Both the stacked standard and object were then extracted using both boxcar (5 pixel) and optimal (Horne 1986) extraction methods, with the latter being the presented spectra.

We then fitted a function to account for the sensitivity, CCD quantum efficiency, and zeropoint. The telluric regions listed by Reiners et al. (2007) and Smette et al. (2015) were masked out. We divided each standard by its corresponding flux calibrated spectrum from the literature, as listed above. This sensitivity function was then applied to the reduced standard and object to flux calibrate the extracted spectra. If an observation had more than one science frame, those were co-added after wavelength and flux calibration.

The standards observed under the R2500I VPHG were used to create a telluric model from a high resolution atmospheric grid derived at Las Campanas. This grid was interpolated through to find the best match across airmass and precipitable water vapour. The telluric model was applied back to the flux calibrated standard and object. This telluric corrected standard was visually checked to confirm that the telluric model was behaving appropriately. The configuration files used in our reduction procedure are given in Appendix A6.

It is important to mention here that we made a comparison between this `PYPEIT` reduction and that of a customized reduction (both the full basic image and spectral reductions) using standard `IRAF`tasks. This was done with the aim of validating the quality of the `PYPEIT` data against that from a well proven reference source. In Appendices A2 and A3 we describe this procedure in detail for one suitably chosen test object from our selection sample, and which is common to both independent reductions: J1745−1640.

A comparison between the `PYPEIT` reduction, and that which used standard `IRAF` routines, is shown in the normalized spectra of J1745−1640 in Fig. 1. We show good agreement in the flux profile up to ∼8900 Å. The `IRAF` reduced spectra is brighter in the broad H_2O region due to the differing telluric correction methods. The MagE spectrum was not telluric corrected whilst the `IRAF` spectrum was telluric corrected using a blackbody, instead of Ross 640 (the corresponding white dwarf standard). This difference does not affect the model fitting of the spectra, as this is done in localized, small, chunks. All spectra then agree at wavelengths $\gtrapprox$9800 Å.

4 ANALYSIS

Here, we discuss the analysis of the reduced spectra, in order to produce spectral types, astrophysical parameters, and kinematics. We discuss our measurements of astrophysical parameters first because the cross-correlation technique used to measure RV requires the use of a best-fitting model derived template, obtained from the best fit of astrophysical parameters. The code used for both estimating astrophysical parameters and calculating RV is `RVFITTER` (Cooper 2022b). This program was developed to effectively recreate in `PYTHON` older codes (e.g. `IRAF.FXCORR`, `IRAF.SPLOT`, `IDL.GAUSSFIT`) designed for allowing a user to manually cross-correlate spectra and fit line centres with different profiles. All wavelengths discussed in this section are in standard air, hence we converted our `PYPEIT` spectra from vacuum to air. This was performed via the `SPECUTILS` package, using the corrections by Edlen (1953).

[6]https://github.com/pypeit/PypeIt

Table 3. Our spectral types compared with the literature optical and near-infrared types for each object.

Object short name	Lit Opt sp. type	Lit NIR sp. type	By eye sp. type	`kastredux` sp. type	Object short name	Lit Opt sp. type	Lit NIR sp. type	By eye sp. type	`kastredux` sp. type
J0028−1927	L0:[1]	L0.5[2]	L0.5	L1	J0235−0849	L2[3]	L2:[2]	L2	L2
J0428−2253	L0.5[4]	L0[2]	L0.5	L1	J0453−1751	L3:[5]	L3[2]	L3β	L3
J0502+1442	L0[6]	M9[2]	M9β	L0	J0605−2342	L0:[7]	L1:[2]	L0.5	L1
J0741+2316	L1[8]	...	L0	L0	J0752+4136	M7[9]	...	M6	M6
J0809+2315	...	...	L4:	L4	J0823+0240	...	...	M9	M8
J0823+6125	L2:[1]	L2.5[2]	L3	L3	J0847−1532	L2[5]	...	L2	L2
J0918+2134	L2.5[10]	L2.5[2]	L3	L3	J0935−2934	L0[1]	L0.5[2]	L0	L0
J0938+0443	L0[6]	M8[2]	M9	M8	J0940+2946	L1[6]	L0.5[2]	...	L2
J0953−1014	L0[7]	M9.5[2]	M9.5β	L0	J1004+5022	L3Vl-G[11]	L3Int-G[12]	L3β	L4
J1004−1318	L0[13]	L1:[14]	L3.5β	L3	J1047−1815	L2.5[15]	L0.5[2]	L1	L1
J1058−1548	L3[10]	L3[16]	L3β	L3	J1109−1606	L0[6]	...	L1	L0
J1127+4705	L1[6]	...	L1	L1	J1213−0432	L5[5]	L4[2]	L5β	L4
J1216+4927	L1[6]	...	L2:	L2	J1221+0257	L0.5[17]	M9p[18]	M9.5	L0
J1222+1407	M9[8]	...	M9::	L0	J1232−0951	L0[1]	M9.5[2]	M9.5	L0
J1246+4027	L4[19]	L4[2]	L4 w/ Li	L4	J1331+3407	L0[1]	L1p(red)[20]	L0	L1
J1333−0215	L3[6]	L2[2]	...	L2	J1346+0842	L2[6]	...	L2.5	L3
J1412+1633	L0.5[19]	L0[2]	L0	L1	J1421+1827	L0[1]	M9[2]	M9.5	L0
J1439+0039	...	...	...	L0	J1441−0945	L0.5[11]	L0.5[2]	L0.5	L1
J1527+0553	...	...	...	L0	J1532+2611	L1[6]	...	...	L3
J1539−0520	L4:[11]	L2[21]	L4.5	L3	J1548−1636	...	L2:[22]	M9.5	L0
J1617+7733B	...	...	...	M6	J1618−1321	L0:[11]	M9.5[2]	L0	L1
J1623+1530	L0[6]	...	M9	L0	J1623+2908	L1[6]	...	L1::	L1
J1705−0516	L0.5[1]	L1[12]	L1	L1	J1707−0138	L0.5[13]	L2[23]	L1	L1
J1717+6526	L4[3]	L6[2]	L6	L5	J1724+2336	...	...	...	L0
J1733−1654	L0.5:[24]	L1[2]	L2	L3	J1745−1640	L1.5:[24]	L1.5[2]	L1	L1
J1750−0016	...	L5.5[22]	L5.5	L4	J2155+2345	...	L2[20]	L3	L2
J2339+3507	L3.5[1]	...	L3.5	L3					

Notes. Literature Spectral Types:
1. Reid et al. (2008),
2. Bardalez Gagliuffi et al. (2014),
3. Hawley et al. (2002),
4. Kendall et al. (2003),
5. Cruz et al. (2003),
6. Schmidt et al. (2010),
7. Cruz et al. (2007),
8. Marocco et al. (2017),
9. West et al. (2011),
10. Kirkpatrick et al. (1999),
11. Kirkpatrick et al. (2008),
12. Allers & Liu (2013),
13. Martín et al. (2010),
14. Marocco et al. (2013),
15. Martín et al. (1999b),
16. Knapp et al. (2004),
17. Schneider et al. (2014),
18. Gagné et al. (2015a),
19. Kirkpatrick et al. (2000),
20. Kirkpatrick et al. (2010),
21. Kendall et al. (2004),
22. Kendall et al. (2007),
23. Phan-Bao et al. (2011),
24. Phan-Bao et al. (2008).

The ':' after a spectral type indicates uncertainty of ±1 whilst 'p' indicates peculiarity. The surface gravity flag β is given when appropriate, and is discussed in Section Section 5.3.1. The adopted spectral type is the `kastredux` method, only overwritten where there are gravity flags in the 'by eye' method. In addition, J1246+4027 has been typed as having a potential Li I detection (λ6708 Å), which can only be seen in the R300R spectra.

4.1 Spectral typing

We spectral typed both the R300R and R2500I spectra using the `CLASSIFYTEMPLATE` method of the `KASTREDUX` (Burgasser 2021) package. This compared each spectrum against SDSS standards (Bochanski et al. 2007; Schmidt et al. 2010; Kesseli et al. 2017), from M0–T0, and selected the spectral type with the minimum difference in scaled fluxes (ΔF: equations 3 and 4) with equally weighted (W) points.

$$\Delta F = \sum \frac{W(F_{\rm object} - K F_{\rm standard})^2}{\sigma^2_{\rm object}} \quad (3)$$

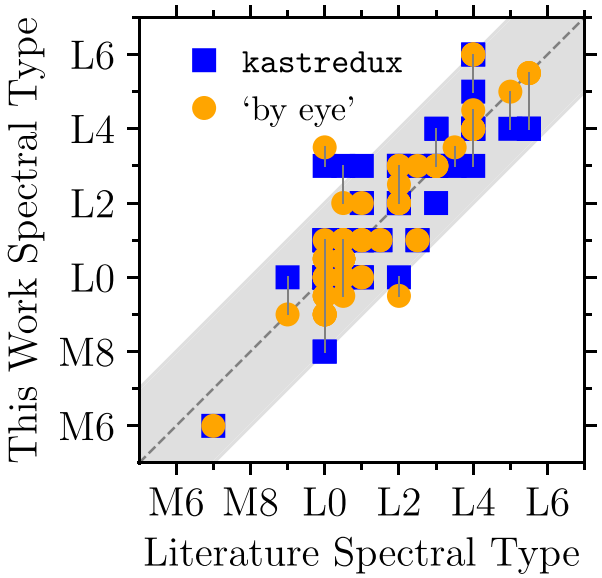

Figure 8. Comparison between this works spectral types and the literature spectral types. Blue squares are spectral types from our adopted, KASTREDUX method whilst orange circles are from the manual 'by eye' method. Grey lines connect these two methods and we show a one-to-one dashed grey line with associated ±2 spectral subtypes confidence bands.

$$K = \sum \frac{W F_{\rm object} F_{\rm standard}}{\sigma^2_{\rm object}} \Bigg/ \sum \frac{W F_{\rm standard} F_{\rm standard}}{\sigma^2_{\rm object}} \quad (4)$$

The spectra had all been smoothed in wavelength with a Gaussian 5σ kernel, and we only compared the regions from 8000 to 8500 Å for R2500I and 7000 to 8000 Å for R300R. This was decided through experimentation, which deliberately excluded regions with telluric features, as those features can cause poorer solutions. Each object was also visually checked against known standards (Kirkpatrick et al. 1999), the spectral sub-types by which we refer to as 'by eye'. Any spectra with indicators of youth are given optical gravity classes as defined by Cruz, Kirkpatrick & Burgasser (2009), from β, γ, δ in order of decreasing surface gravity. The KASTREDUX spectral types were our adopted spectral types.

4.1.1 GTC spectral sequence

The 46 spectra from the R2500I VPHG, ordered by our adopted spectral type, are shown in Figs 2 and 3. All spectra are heliocentric corrected, such that the relative motion of the Earth has been removed. Each spectrum shown had an outlier masking routine applied such that points within a rolling ≈15 Å (ten data points) chunk are removed if they had a difference greater than the standard deviation from the median. Additionally, some objects had problematic O_2 A-band tellurics. In those cases, we interpolated over the region 7540–7630 Å from the maximum of the first ≈7.5 Å to minimum of the last ≈7.5 Å. Where appropriate, spectra were co-added. All spectra appear noisy in the primary H_2O band of ≈9200–9600 Å. The 17 heliocentric corrected, reduced spectra from the R300R grism are shown in Fig. 4. The R300R spectra were trimmed from $6500 < \lambda < 9000$ Å due to (a) the lack of signal in the blue regime and (b) to constrain to purely the first order light. Unlike the R2500I spectra, the R300R spectra were not telluric corrected.

4.2 Fundamental astrophysical parameters

We used the RVFITTER.CROSSCORRELATE code on our R300R and R2500I spectra with BT-Settl CIFIST model grids from $1200 \leq T_{\rm eff} \leq 4000$ K and $4.5 \leq \log g \leq 5.5$ dex (Allard et al. 2011). Lower surface gravity grids were available but not routinely used as the focus was on RV measurement with an a priori expectation of field surface gravity, ≈5 dex. These models assume a solar metallicity with no variation and are linearly dispersed in steps of 100 K and 0.5 dex. This code allowed us to visually select the best-fitting model from the array of model grids and for each spectral line from Table 2.

We used these chosen lines rather than correlating against the entire model because the models do not exactly match the flux profile of ground based spectra. It was also known that the BT-Settl grids were generated using a different line list to our selected alkali lines, taken from the NIST data base (Kramida et al. 2021). For efficiency purposes, each model when being loaded into the code, was interpolated onto the wavelength array of the object being compared against. The models could optionally be Gaussian smoothed, which was helpful for fitting any 'messy' regions of models (e.g. telluric bands in models with $T_{\rm eff} \gtrapprox 2000$ K). We normalized the model and data by their respective medians in a given variably sized 'chunk' around each spectral line. We noted that around certain lines, particular models appeared almost identical to each other, e.g. around 7000–8000 Å, the 1900 and 2000 K models are not visually distinct. This means there is a higher uncertainty for effective temperatures within the 1900–2000 K region. Not every spectral line was used for each object as some have poorly resolved features or low signal-to-noise. Our selected $T_{\rm eff}$ was the mean $T_{\rm eff}$ from each line measurement, as was $\log g$. To determine the error on each $T_{\rm eff}$ and $\log g$ final value, we chose to use the standard deviation from each independent line fit divided by square root of the number of lines used. This error was added in quadrature with half of the separation between each grid, i.e. 50 K for $T_{\rm eff}$ and 0.25 dex for $\log g$.

Additionally, we created an 'expected' effective temperature, $\widehat{T_{\rm eff}}$, using the Filippazzo, sixth-order field $T_{\rm eff}$ relation (Filippazzo et al. 2015) and our adopted spectral types. The errors on $\widehat{T_{\rm eff}}$ correspond with the mean difference in $T_{\rm eff}$ across ±0.5 spectral subtypes (our spectral subtype uncertainty), plus the quoted relation RMS of 113 K.

4.3 Calculating the radial velocities

Only our R2500I spectra were used to determine RVs as the features in R300R spectra are mostly blended/unresolved. We used two methods by which to measure an adopted RV: line centre fitting and cross correlation. We note that our seeing (Table A1, corrected for airmass) was almost always smaller than the slit width, which affects the RV offset as the slit is not fully illuminated. The full width at half-maximum was typically 3–4 pixels, corresponding to ≈0.75–1 arcsec. Most observations were seeing-limited, whilst a few, taken in poorer conditions, were slit-limited. The following methods were performed only on heliocentric corrected spectra, hence any quoted RV values are heliocentric corrected.

4.3.1 Line centre fitting

Using the same atomic absorption lines listed in Table 2, we applied the RVFITTER.LINECENTERING code to interactively fit Gaussian, Lorentzian, and Voigt profiles with the minimum possible width. This minimum possible width is equal to the number of free

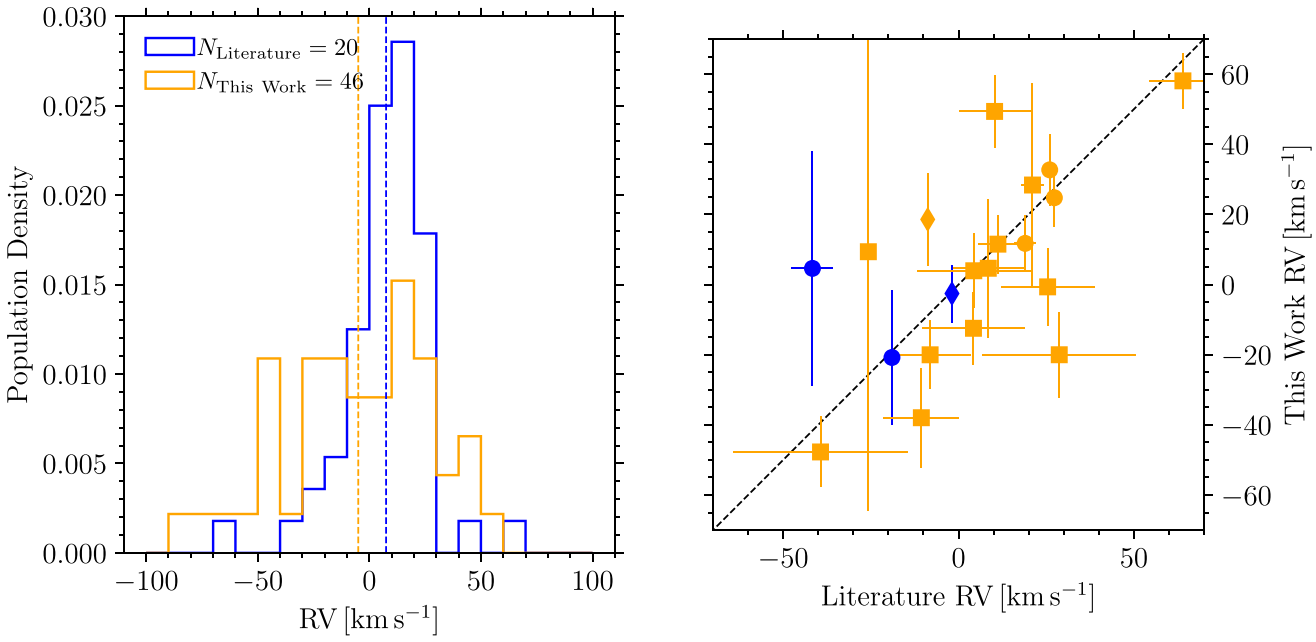

Figure 9. [Left panel]: Histograms of the RVs calculated in this work (orange) and from the literature (blue) to show the relevant population densities. The dashed vertical lines indicate the means of the associated distributions. [Right panel]: The RV values from the literature on the x axis with our adopted RV values, on the y. We show a one-to-one relation, over which our 20 comparison RVs are plotted. Squares are from low-resolution literature measurements, whereas circles and diamonds are mid- and high-resolution literature measurements, respectively. Orange points are like-for-like comparisons and blue points are for the three benchmark systems, i.e. comparisons between our measured secondary RV against the literature RV of the primary.

parameters plus one (although this does not guarantee a successful fit). We used these different profiles to obtain the best fit for a particular line given its underlying absorption characteristics and the available signal-to-noise of the spectral region. The fitting technique used was least-mean-square[7] minimization. For each spectral line, we subtracted a linear continuum from the data. The continuum corresponds to the medians of selected regions to the blueward and redward sides of the spectral line. Each continuum region is chosen to follow the shape of the spectra with a minimum width of ≈50 Å within 100–200 Å of the spectral line. Also shown during the fitting routine is a fifth-order spline, as a visual aid; the minima of the spline does not necessarily correspond to the line position. An example of this routine is given for J1745−1640 in Fig. 5. The fits were only accepted if they appeared to accurately represent the spectral lines profile upon visual inspection. In general, the most consistently reliable lines were the rubidium lines, sodium doublet, and first caesium line. The potassium doublet often was affected by rotational broadening whilst the second caesium line was often affected by neighbouring features. The uncertainty for each line was the value in the diagonal of the covariance matrix corresponding to centroid position from the least-squares fit, plus the wavelength calibration RMS for that object, Doppler shifted into RV space.

After measuring every line, we then calculated the overall weighted mean ($\mu_{\rm LC}$) and weighted standard deviation ($\sigma_{\rm LC}$), the weights were the inverse of the uncertainties of each line used, squared. The uncertainty from the vacuum to air conversion was negligible ($\ll$0.1 km s^{-1}) compared to the fitting uncertainties calculated from the eight (or less, if rejected) aforementioned lines. The final line centre RV standard error was the weighted standard deviation divided by the square root of the number of lines fit.

[7] https://docs.scipy.org/doc/scipy/reference/generated/scipy.optimize.leastsq.html##scipy.optimize.leastsq

4.3.2 *Cross-correlation*

In addition to estimating the astrophysical parameters with `RVFITTER.CROSSCORRELATE` in Section 4.2, we also used the same package to measure RV by manually shifting the best-fitting BT-Settl model as a template. No smoothing was applied to the model template to match the spectral resolution of the object spectrum. This was because smoothing could confuse where the centroid of a line was, when looking by-eye. Likewise, there was no continuum subtraction applied to the object spectrum. The RV shift was in steps of 5, 10, 100 km s^{-1}, which in turn defined the RV uncertainty on each line (2.5, 5, 50 km s^{-1}, i.e. the margin of error). These RV errors are added to the wavelength calibration RMS for the given object (Doppler shifted into an RV error). Not all atomic lines were always used, only in the cases where the model appeared to closely match the apparent line profile. The typical technique was to select a broad region ($\Delta\lambda$ = 100–200 Å) around each spectral line, find the best-fitting template in terms of $T_{\rm eff}$ and log g, then narrow that region ($\Delta\lambda \approx 50$ Å) to then find an RV. This was a predominantly by-eye technique, although root-mean-square deviation divided by interquartile range (RMSDIQR) values were computed as a numerical guide when comparing models. We also show a fifth-order spline, as with the line centring method, as a visual aid. This initial broad region is shown for J1745−1640 in Fig. 6.

As in Section 4.3.1, the overall cross-correlated weighted mean RV value ($\mu_{\rm XC}$) and weighted standard deviation ($\sigma_{\rm XC}$) was calculated using all of the manually selected lines. We used the same method

Table 4. RVs measured in this work and compared to the literature.

Object short name	Literature RV ($km\,s^{-1}$)	Line centre RV ($km\,s^{-1}$)	Cross correlation RV ($km\,s^{-1}$)	Adopted RV ($km\,s^{-1}$)
J0028−1927	...	18.6 ± 7.7^{11111110}	26.3 ± 13.2^{11111111}	20.4 ± 14.9
J0235−0849	15.3 ± 11.2[1], 22.8 ± 6.1[2]	30.9 ± 27.8^{00110111}	26.7 ± 21.0^{00111111}	28.4 ± 29.1
J0428−2253	...	69.3 ± 36.3^{11111110}	16.0 ± 6.1^{00011111}	17.0 ± 12.3
J0453−1751	...	15.1 ± 2.3^{00010110}	13.3 ± 5.9^{00111111}	15.0 ± 8.3
J0502+1442	...	41.3 ± 5.8^{11101110}	41.2 ± 5.4^{11111111}	41.3 ± 10.7
J0605−2342	...	23.4 ± 6.3^{00011110}	25.0 ± 8.8^{11111111}	23.7 ± 11.1
J0741+2316	...	31.1 ± 0.2^{00011000}	38.0 ± 3.3^{11001110}	31.1 ± 7.8
J0752+4136	8.5 ± 10.1[1]	-3.0 ± 19.9^{01001100}	14.2 ± 15.7^{11111100}	4.7 ± 19.7
J0809+2315	...	-48.2 ± 3.2^{00011110}	-38.0 ± 9.5^{00011111}	-47.4 ± 8.9
J0823+0240	...	-26.6 ± 3.8^{00001110}	-4.3 ± 4.5^{11111110}	-21.4 ± 8.8
J0823+6125	...	$-22.6 \pm 11.3^{00011110}$	$-12.9 \pm 12.7^{10111111}$	-19.6 ± 15.4
J0918+2134	...	-92.9 ± 7.3^{00001110}	-80.0 ± 7.5^{00111110}	-88.2 ± 10.6
J0935−2934	...	-3.7 ± 13.2^{10001110}	-22.5 ± 6.1^{11111111}	-16.9 ± 12.8
J0938+0443	25.4 ± 13.3[1]	2.7 ± 7.2^{00011110}	-5.7 ± 6.7^{11111101}	-0.7 ± 11.1
J0940+2946	27.3 ± 11.8[1], 4.1 ± 7.1[2]	51.6 ± 5.1^{00011110}	35.0 ± 9.2^{11111111}	49.4 ± 10.3
J0953−1014	...	63.2 ± 7.9^{01000011}	10.0 ± 7.5^{11111111}	47.6 ± 11.3
J1004+5022	-1.7 ± 1.5†[3], -1.6 ± 0.9†[4], -0.7 ± 1.2†[5], -2.8 ± 0.9†[6]	1.1 ± 11.4^{00000100}	-3.0 ± 1.8^{00011111}	-2.6 ± 8.2
J1004−1318	...	22.4 ± 5.9^{00111110}	13.3 ± 8.4^{00111111}	19.7 ± 11.1
J1047−1815	...	-17.2 ± 4.6^{00001111}	-18.0 ± 6.6^{00011111}	-17.4 ± 9.6
J1058−1548	...	-0.5 ± 9.9^{00011111}	-1.0 ± 5.7^{00011111}	-0.9 ± 11.1
J1109−1606	48.7 ± 16.1[1], 69.9 ± 10.0[2]	58.5 ± 1.2^{00000011}	48.7 ± 2.8^{11111111}	58.1 ± 7.9
J1127+4705	-23.7 ± 11.1[1], -26.4 ± 6.5[2]	8.9 ± 62.3^{00011110}	10.0 ± 69.3^{00011110}	9.4 ± 73.7
J1213−0432	...	$-20.6 \pm 17.0^{00011110}$	$-40.0 \pm 24.7^{00111111}$	-25.3 ± 22.4
J1216+4927	4.3 ± 16.2[1]	2.2 ± 4.1^{11111111}	8.8 ± 6.9^{11111111}	3.9 ± 10.6
J1221+0257	2.0 ± 10.1[1], -8.0 ± 3.0[7], -12.6 ± 4.1[2], -8.8 ± 0.1[8]	17.5 ± 7.0^{11111111}	20.0 ± 8.1^{11111111}	18.6 ± 13.2
J1232−0951	...	1.8 ± 8.1^{11111111}	-8.6 ± 7.3^{11111110}	-4.2 ± 13.1
J1246+4027	...	$-46.7 \pm 12.5^{00111111}$	$-46.7 \pm 15.0^{00111111}$	-46.7 ± 18.3
J1331+3407	4.1 ± 10.2[1], 15.4 ± 7.8[2]	-5.6 ± 24.0^{00000100}	12.0 ± 1.8^{00011111}	11.5 ± 8.3
J1333−0215	28.7 ± 21.8[1]	-29.2 ± 7.2^{00111111}	-7.5 ± 7.2^{11111111}	-20.0 ± 12.2
J1346+0842	-67.9 ± 12.2[1], -17.7 ± 10.6[2]	-50.7 ± 4.0^{00111111}	-35.6 ± 7.0^{11111111}	-47.7 ± 10.0
J1412+1633	...	$-63.4 \pm 15.9^{11111100}$	$-81.4 \pm 20.5^{11111111}$	-70.8 ± 25.8
J1421+1827	...	-12.6 ± 9.6^{11111110}	-10.0 ± 9.1^{11011110}	-11.2 ± 14.2
J1441−0945	-41.6 ± 5.9†[4]	-1.3 ± 53.8^{00001001}	8.0 ± 25.8^{00111011}	4.6 ± 33.4
J1532+2611	-38.8 ± 36.6[1], 9.2 ± 12.4[2]	-15.6 ± 9.4^{00011111}	-11.7 ± 4.4^{00111111}	-12.5 ± 10.3
J1539−0520	27.3 ± 0.2[9], 27.0 ± 4.0[7]	36.7 ± 7.4^{00011011}	24.0 ± 1.7^{00011111}	24.8 ± 8.2
J1548−1636	...	11.8 ± 6.3^{11111111}	21.3 ± 7.4^{11111111}	15.8 ± 12.4
J1617+7733B	-19.0 ± 0.8†[4]	$-31.6 \pm 24.5^{00011111}$	$-18.0 \pm 12.5^{10011110}$	-20.8 ± 19.2
J1618−1321	...	-39.5 ± 9.8^{00011111}	$-75.0 \pm 48.0^{00101101}$	-41.2 ± 17.0
J1623+1530	-17.8 ± 11.5[1], 5.4 ± 17.2[2]	$-50.2 \pm 10.4^{00111111}$	-28.7 ± 7.8^{11111111}	-38.0 ± 14.1
J1623+2908	-8.1 ± 11.5[2]	-18.8 ± 5.3^{00000111}	-26.0 ± 9.2^{00011111}	-20.0 ± 9.8
J1707−0138	...	25.2 ± 7.3^{11111111}	18.3 ± 9.5^{00111111}	22.2 ± 13.5
J1717+6526	...	-62.6 ± 3.3^{00111111}	-76.7 ± 6.1^{00111111}	-64.4 ± 8.7
J1745−1640	26.0 ± 2.0[7]	36.2 ± 4.4^{11111111}	28.8 ± 4.7^{11111111}	32.7 ± 10.1
J1750−0016	19.0 ± 3.0[7]	1.5 ± 2.9^{00110110}	16.0 ± 1.7^{00110111}	11.7 ± 8.1
J2155+2345	...	$-47.6 \pm 12.6^{00111111}$	$-46.7 \pm 11.0^{00111111}$	-47.1 ± 16.3
J2339+3507	...	$-60.0 \pm 10.9^{00011110}$	$-47.1 \pm 10.4^{01111111}$	-55.1 ± 14.4

Notes. Literature Radial Velocities:
1. Kiman et al. (2019),
2. Schmidt et al. (2010),
3. Binks & Jeffries (2016),
4. Gaia Collaboration et al. (2018a),
5. Shkolnik et al. (2012),
6. Schlieder, Lépine & Simon (2012b),
7. Burgasser et al. (2015),
8. Hsu et al. (2021),
9. Blake et al. (2010).

Indices: 1 if line from Table 2 used, 0 otherwise.

Quoted RVs are already heliocentric corrected. A '†' symbol next to an RV means the RV is that of the primary star in the common proper motion system a given object is part of.

Table 5. The UVW velocities and BANYAN Σ classification (with associated probability) from this work.

Object short name	V_{tan} (km s^{-1})	V_r (km s^{-1})	U (km s^{-1})	V (km s^{-1})	W (km s^{-1})	V_{total} component	Galaxy component	BANYAN Σ classification	Probability (per cent)
J0028−1927	20.5	20.4	10.7	10.1	−14.8	20.9	Thin	Field	100.0
J0235−0849	6.0	28.4	3.0	18.0	−19.8	26.9	Thin	Field	100.0
J0428−2253	23.3	17.0	19.5	7.0	9.7	22.9	Thin	Field	100.0
J0453−1751	7.0	15.0	0.6	0.2	2.2	2.3	Thin	β Pictoris	98.9
J0502+1442	17.1	41.3	32.1	−5.1	4.7	32.8	Thin	Hyades	99.1
J0605−2342	19.4	23.7	18.3	9.9	−7.8	22.2	Thin	Field	100.0
J0741+2316	10.1[1]	31.1	22.9	4.3	8.1	24.7	Thin	Field	99.9
J0752+4136	10.3	4.7	−0.7	19.8	1.5	19.9	Thin	Field	100.0
J0823+6125	61.6	−19.6	17.3	−9.8	−48.1	52.1	Thin	Field	100.0
J0847−1532	19.8	−1.0[2]	−26.2	4.5	5.6	27.2	Thin	Field	100.0
J0935−2934	11.1	−16.9	−3.6	32.9	8.8	34.3	Thin	Field	100.0
J0938+0443	13.1	−0.7	−13.4	3.2	−0.3	13.8	Thin	Field	100.0
J0940+2946	38.2	49.4	46.3	−14.0	18.7	51.8	Thin	Field	100.0
J0953−1014	18.0	47.6	11.1	−32.3	17.3	38.3	Thin	Field	98.4
J1004+5022	25.3	−2.6	0.7	−9.6	0.7	9.6	Thin	Field	99.8
J1004−1318	27.1	19.7	−4.9	−17.9	−5.0	19.2	Thin	Field	66.5
J1047−1815	49.0	−17.4	34.9	17.6	−21.8	44.8	Thin	Field	100.0
J1058−1548	22.4	−0.9	11.9	8.9	−1.7	14.9	Thin	Argus	93.1
J1109−1606	105.0	58.1	43.3	−90.0	−25.7	103.1	Thick	Field	100.0
J1127+4705	13.2	9.4	2.8	4.2	13.6	14.5	Thin	Field	100.0
J1213−0432	29.6	−25.3	19.5	10.8	−20.5	30.2	Thin	Carina Near	72.0†
J1221+0257	13.3	18.6	−1.4	−3.4	20.3	20.6	Thin	Field	100.0
J1232−0951	30.2[3]	−4.2	6.6	−8.3	−8.9	13.8	Thin	Field	99.8
J1246+4027	17.6	−46.7	−32.3	3.0	−36.1	48.5	Thin	Field	100.0
J1331+3407	55.8	11.5	14.6	−33.9	28.4	46.6	Thin	Field	100.0
J1333−0215	52.5	−20.0	27.3	−25.2	−13.2	39.4	Thin	Field	100.0
J1346+0842	52.6	−47.7	35.2	−25.8	−33.5	55.0	Thin	Field	100.0
J1412+1633	17.9	−70.8	4.5	−2.0	−63.7	63.9	Thin	Field	100.0
J1421+1827	69.2	−11.2	32.2	−42.8	16.7	56.1	Thin	Field	100.0
J1441−0945	30.7	4.6	6.5	−9.9	20.6	23.8	Thin	Field	63.1
J1539−0520	47.9	24.8	−46.2	51.0	−2.1	68.8	Thin	Field	100.0
J1548−1636	30.3	15.8	−14.9	−17.0	20.8	30.7	Thin	Field	100.0
J1617+7733B	18.7	−20.8	1.5	−11.4	−1.8	11.7	Thin	Field	96.0
J1618−1321	29.3[4]	−41.2	31.5	−15.5	−4.6	35.4	Thin	Field	100.0
J1623+1530	14.7	−38.0	14.3	−14.9	−11.8	23.8	Thin	Field	100.0
J1705−0516	14.9	12.2[5]	−25.4	14.2	−2.8	29.2	Thin	Field	100.0
J1707−0138	5.8	22.2	−30.5	19.1	9.7	37.3	Thin	Field	100.0
J1717+6526	20.1	−64.4	−27.4	−30.5	−41.2	58.1	Thin	Field	100.0
J1733−1654	7.0	17.0[2]	−26.1	16.5	2.1	31.0	Thin	Field	100.0
J1745−1640	13.7	32.7	−42.5	16.7	−3.2	45.7	Thin	Field	100.0
J1750−0016	19.4	11.7	−15.0	15.9	28.1	35.6	Thin	Field	100.0
J2339+3507	23.4	−55.1	−4.1	−44.6	20.6	49.3	Thin	Field	100.0

Notes. Literature astrometry used to generate UVWs:
1. Smith et al. (2014),
2. Burgasser et al. (2015),
3. Best et al. (2020),
4. Weinberger et al. (2016),
5. Blake et al. (2010).
U is in the direction of the Galactic anticentre. Derived using this work's adopted radial velocity in combination with *Gaia* DR3 kinematics unless otherwise indicated. We also show the predicted Galaxy component, taken from the UVW velocities and V_{total} cuts in Nissen & Schuster (2010).
†: J1213−0432 had an additional probability (26 per cent) of being a member of Argus, for a total non-field probability of 98 per cent.

to estimate the uncertainty in final cross-correlation derived RVs as for the line centre results, by finding the standard error of the mean.

4.3.3 Adopted RV

We created an adopted RV by constructing a weighted mean, using the deviation in each method as the weighting. The different RV values for each line, method, and the corresponding probability distribution functions (PDFs) are shown in Fig. 7, for J1745−1640. We also note that our final adopted RV for J1745−1640 obtained from combining the results of the two measurement techniques (32.7 ± 6.5 km s^{-1}) is in agreement with the values obtained from both the customized IRAF reduced data and the value reported by Burgasser et al. (2015), within their respective uncertainties. See Appendix A3 for a full description.

The adopted RV was the mean (μ_{RV}) whilst the standard error (δ_{RV}) was equal to the standard deviation (σ_{RV}) divided by $\sqrt{2}$. The mean and standard deviation was calculated through the inverse variance

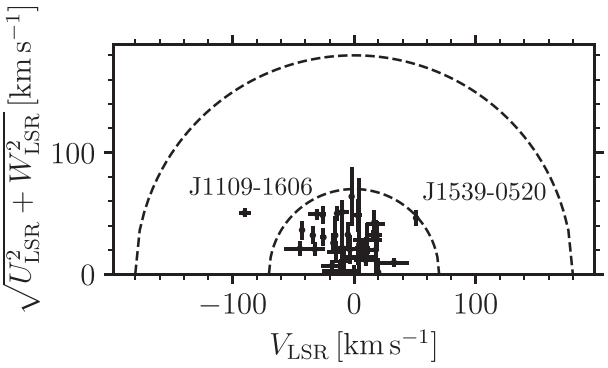

Figure 10. Toomre diagram, as done by Bensby et al. (2005), using *Gaia* DR3 astrometry in combination with our calculated RVs. V is on the x axis, against the velocity dispersion ($\sqrt{U^2 + W^2}$) on the y axis. Black circles are UVW velocities calculated with the RVs from this work, with associated error-bars given. We show the respective thick disc and halo selection lines at $V_{\rm total} > 70\,{\rm km\,s^{-1}}$ and $V_{\rm total} > 180\,{\rm km\,s^{-1}}$, respectively.

weighting equations (5) and (6). Typically, we found that the cross-correlation technique was more precise (being more controlled by-eye) and robust. The line centre fitting was often more accurate, however, and performed best on the higher quality spectra.

$$\mu_{\rm RV} = \frac{\mu_{\rm LC}\sigma_{\rm XC}^2 + \mu_{\rm XC}\sigma_{\rm LC}^2}{\sigma_{\rm LC}^2 + \sigma_{\rm XC}^2} \quad (5)$$

$$\sigma_{\rm RV} = \sqrt{\frac{\sigma_{\rm LC}^2\sigma_{\rm XC}^2}{\sigma_{\rm LC}^2 + \sigma_{\rm XC}^2}} \quad (6)$$

4.4 Kinematics

Galactic UVW velocities were calculated using our adopted RVs plus *Gaia* astrometric measurements, using the equations from `ASTROLIBPY`. We corrected for the Local Standard of Rest (LSR) using the values from Coşkunoğlu et al. (2011) where U, V, W $= (-8.50, +13.38, +6.49)\,{\rm km\,s^{-1}}$. These equations follow the work by Johnson & Soderblom (1987), except that U is orientated towards the Galactic anticentre. We also used BANYAN Σ(Gagné et al. 2015a, 2018), which provided moving group classification with associated probability. When using BANYAN Σ, we checked the resultant probabilities both with and without RV. This was because RV has by far the lowest precision, thus could reduce a likely membership candidate into a field object in error. Our final values are the ones which include RV. Notably, when using velocities in the Galactic reference frame, one can select a Galactic component with $V_{\rm total}$ (where $V_{\rm total}$ is the total space velocity, $V_{\rm total} = \sqrt{U^2 + V^2 + W^2}$). We followed the work by Nissen & Schuster (2010) and define thick disc and halo objects as having $V_{\rm total} > 70\,{\rm km\,s^{-1}}$ and $V_{\rm total} > 180\,{\rm km\,s^{-1}}$, respectively. This definition, especially for separating the thin and thick disc, is indicative of metallicity; see the Besançon Galaxy models (Czekaj et al. 2014; Lagarde et al. 2021).

5 RESULTS

In this section, we present the spectral types, radial velocities, and astrophysical parameters. In Table A2, we provide photometry from the *Gaia*, 2MASS, and ALLWISE catalogues. We discuss individually interesting objects and objects where our measured results differ significantly from published values.

5.1 Spectral types

In Table 3 we list published spectral types based on optical spectra, near-infrared spectra, and the 'by eye' and `KASTREDUX` methods discussed in Section 4.1. This work has produced the first spectral type estimates for six of the 53 objects.

The 47 objects with known spectral types have a standard deviation of 0.5 subtypes between the published values and the 'by eye'/`KASTREDUX` results, which we adopt as the error on the new spectral subtypes. When the literature values for a given object differ we adopted the optical spectral type. Our spectral types across the two methods are displayed against the adopted literature spectral types in Fig. 8.

All objects except J1004−1318 have subtype differences between the spectral type derived in this work and the adopted literature spectral type of less than two subtypes. J1004−1318, has an optical (Opt) spectral subtype of L0 (Martín et al. 2010) whilst Marocco et al. (2013) found a subtype of L1 using near-infrared (NIR) spectra; we find a subtype of L3. However, a more recent study, Robert et al. (2016), found a subtype of L4 (NIR), which is more consistent with our result. The fit statistic from `KASTREDUX` is about twice larger for L1 than for L3. In Fig. 2, J1004−1318 does not seem dissimilar to the neighbouring objects, whereas the L0/L1 spectra appear different (e.g. weaker alkali lines). The different spectral typing of J1004−1318 may be due to lower signal-to-noise (S/N) ratios of some observations. For example, Martín et al. (2010) exposed for 2400 s at the 2.56 m Nordic Optical Telescope, while we exposed for 1500 s, and with moderately good seeing and low airmass, with a telescope with an aperture over 16 times larger.

5.2 Radial velocity analysis

We have derived RVs for 46 of the observed 53 objects, the seven objects that we did not measure RVs were only observed with the R300R grism. For 20 of the 53 objects, there are published RVs and for 17 of these we have measured RVs. The objects J1004+5022, J1441−0945, and J1617+7733B are candidate members of benchmark systems (Section 2.1), and we adopt the RVs of their primary stars as a comparison with our measured values for the secondary, for a total of 20 comparison RVs. In Fig. 9, we plot histograms of the 20 published and the 46 measured values. We also show the difference between the published and measured values of the 20 overlapping objects. If there is more than one literature value, we take the weighted mean RV and standard error on the mean, to compare against the adopted RV from this work. We show literature measurements with respect to their resolutions and define these as: low, $R < 2\,500$; mid, $2\,500 \leq R \leq 25\,000$; high, $R > 25\,000$. The error used to define σ are the quadrature summed errors from the literature and our adopted RV.

Our 46 RVs in the heliocentric reference frame are presented in Table 4. This reference frame has been experimented with, in that the heliocentric/barycentric correction via `PYPEIT` has been compared with a manual barycentric correction using `BARYCORRPY` (Kanodia & Wright 2018). Resultant RV differences from the manual barycentric correction to the pipeline barycentric correction differ by $\approx 0.1\,{\rm km\,s^{-1}}$. The difference between heliocentric and barycentric correction is $0.5\,{\rm km\,s^{-1}}$ in the case of J1745−1640.

The median difference between our adopted RVs and the literature RVs was $7.8\,{\rm km\,s^{-1}}$. This $7.8\,{\rm km\,s^{-1}}$ was then added in quadrature to our adopted RV error. We used this value to account for systematic uncertainties such as night-to-night instrumental drift and any FWHM

Table 6. Effective temperatures and surface gravities from this work.

Object short name	$\widehat{T_{\rm eff}}$ (K)	$T_{\rm eff}$ (K)	*Gaia*$T_{\rm eff}$ (K)	log g (dex)	Object short name	$\widehat{T_{\rm eff}}$ (K)	$T_{\rm eff}$ (K)	*Gaia*$T_{\rm eff}$ (K)	log g (dex)
J0028−1927	2102±185	1988±116	2115±112	4.8±0.4	J0235−0849	1959±183	1983±62	2035±190	5.0±0.3
J0428−2253	2102±185	1980±64	2322±71	5.0±0.3	J0453−1751	1822±179	1850±70	1921±176	5.0±0.3
J0502+1442	2249±186	2212±126	2285±80	4.9±0.3	J0605−2342	2102±185	2088±136	2121±82	4.8±0.4
J0741+2316	2249±186	2020±190	...	5.0±0.3	J0752+4136	2831±189	2817±62	...	4.9±0.4
J0809+2315	1695±173	1820±64	...	5.5±0.3	J0823+0240	2539±184	2500±287	...	5.1±0.4
J0823+6125	1822±179	1843±70	1951±93	4.7±0.4	J0847−1532	1959±183	1950±70	2040±50	5.0±0.3
J0918+2134	1822±179	1880±110	...	5.2±0.4	J0935−2934	2249±186	2162±121	2316±39	5.0±0.3
J0938+0443	2539±184	2486±228	2364±88	5.1±0.4	J0940+2946	1959±183	1950±70	2144±164	4.6±0.4
J0953−1014	2249±186	2100±150	2181±70	4.6±0.4	J1004+5022	1695±173	1740±70	1899±100	4.5±0.3
J1004−1318	1822±179	1850±70	1886±197	5.0±0.3	J1047−1815	2102±185	1980±64	2103±81	5.0±0.3
J1058−1548	1822±179	1900±102	1834±109	5.0±0.3	J1109−1606	2249±186	2175±82	2104±112	5.0±0.3
J1127+4705	2102±185	2060±94	2136±120	4.9±0.4	J1213−0432	1695±173	1783±143	1580±152	5.0±0.3
J1216+4927	1959±183	2012±59	...	4.8±0.4	J1221+0257	2249±186	2250±295	2210±41	5.0±0.3
J1222+1407	2249±186	2150±70	...	5.0±0.3	J1232−0951	2249±186	2114±144	...	5.0±0.3
J1246+4027	1695±173	1750±91	1780±162	4.6±0.4	J1331+3407	2102±185	2040±70	2170±71	4.9±0.4
J1333−0215	1959±183	2075±96	2104±76	4.8±0.4	J1346+0842	1822±179	1888±78	1889±349	4.8±0.4
J1412+1633	2102±185	2014±97	2104±55	4.6±0.4	J1421+1827	2249±186	2133±157	2233±69	4.9±0.4
J1439+0039	2249±186	2325±139	...	5.0±0.3	J1441−0945	2102±185	2060±94	2240±60	4.9±0.4
J1527+0553	2249±186	2100±50	...	5.0±0.3	J1532+2611	1822±179	1917±84	...	4.8±0.4
J1539−0520	1822±179	1840±70	1804±109	5.4±0.4	J1548−1636	2249±186	2125±147	2272±82	4.9±0.3
J1617+7733B	2831±189	2860±94	...	4.9±0.4	J1618−1321	2102±185	2050±100	...	5.0±0.3
J1623+1530	2249±186	2112±105	2339±147	4.8±0.4	J1623+2908	2102±185	2080±90	...	5.2±0.4
J1705−0516	2102±185	1950±70	2065±35	5.0±0.3	J1707−0138	2102±185	2100±180	2019±78	5.0±0.3
J1717+6526	1581±166	1550±168	1589±63	4.7±0.4	J1724+2336	2249±186	2550±70	2320±88	5.0±0.3
J1733−1654	1822±179	1800±50	2055±63	4.8±0.4	J1745−1640	2102±185	2088±105	2008±49	5.0±0.3
J1750−0016	1695±173	1660±113	1542±71	5.1±0.4	J2155+2345	1959±183	1900±76	...	5.0±0.3
J2339+3507	1822±179	1871±86	1855±138	5.0±0.3					

Note. These $T_{\rm eff}$ values are generated using fits to preferentially R2500I spectra if available, else R300R. Model fits assume solar metallicities. $\widehat{T_{\rm eff}}$ represents the expected effective temperature, based on an object's spectral type. *Gaia*$T_{\rm eff}$ are the `teff_espucd` effective temperatures from *Gaia* DR3.

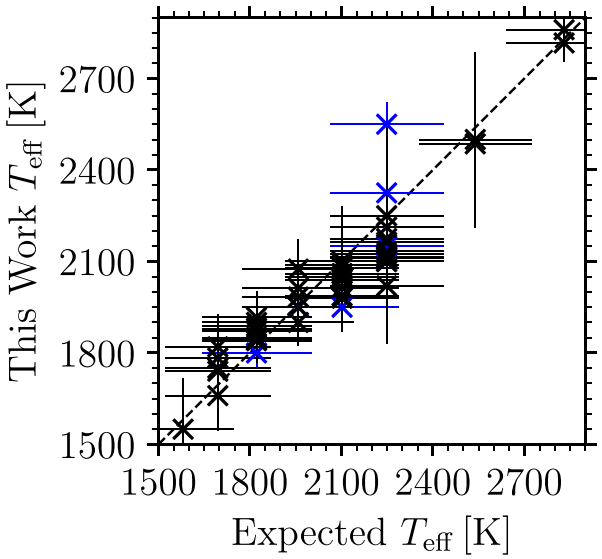

Figure 11. The expected $\widehat{T_{\rm eff}}$ (calculated via spectral type through a Filippazzo relation; Filippazzo et al. 2015) on the x axis and the best-fitting BT-Settl model mean $T_{\rm eff}$ on the y axis. Blue crosses are for objects with a fit to the R300R spectra whilst black crosses are objects with a fit to the R2500I spectra.

undersampling. A S/N ratio of 20–30 also correlates with an RV uncertainty of ≈8 km s^{-1}, which was the typical S/N ratio seen around our alkali lines. Some lines, such as the potassium doublet, had lower S/N ratios and lower local resolutions due to a combination of wider features and lower flux values. All objects except J0940+2946 and J1221+0257 have an adopted and literature RV difference less than twice the sum of the respective errors in quadrature. J0940+2946 was 2.69σ from the weighted mean literature value. Of the two literature values constructing this weighted mean, our value is <2σ from the value from Kiman et al. (2019), which is notably larger than the value from Schmidt et al. (2010). J1221+0257 was 2.08σ from the weighted mean literature value. Our RV value was closest to the value from Kiman et al. (2019), with less agreement shown with the value from Schmidt et al. (2010), which itself was most similar to the values from Burgasser et al. (2015) and Hsu et al. (2021). We note for both of these objects that the RV values from Schmidt et al. (2010) utilized considerably lower resolution spectra, hence a worse agreement being shown. Any objects in Table 4 which have known primary stars with literature RVs are discussed below:

J1004+5022: G 196–3B is the binary companion to G 196–3A (Kirkpatrick et al. 2008). G 196–33A has a mean RV of -1.6 ± 0.4 km s^{-1}(Shkolnik et al. 2012; Schlieder et al. 2012b; Binks & Jeffries 2016; Gaia Collaboration 2018a). This mean RV of the primary is 0.1σ away from the RV of the secondary companion from this work.

J1441−0945: DENISJ144137.2−094558 is the binary companion to G 124–62 (Bouy et al. 2003; Seifahrt, Guenther & Neuhäuser

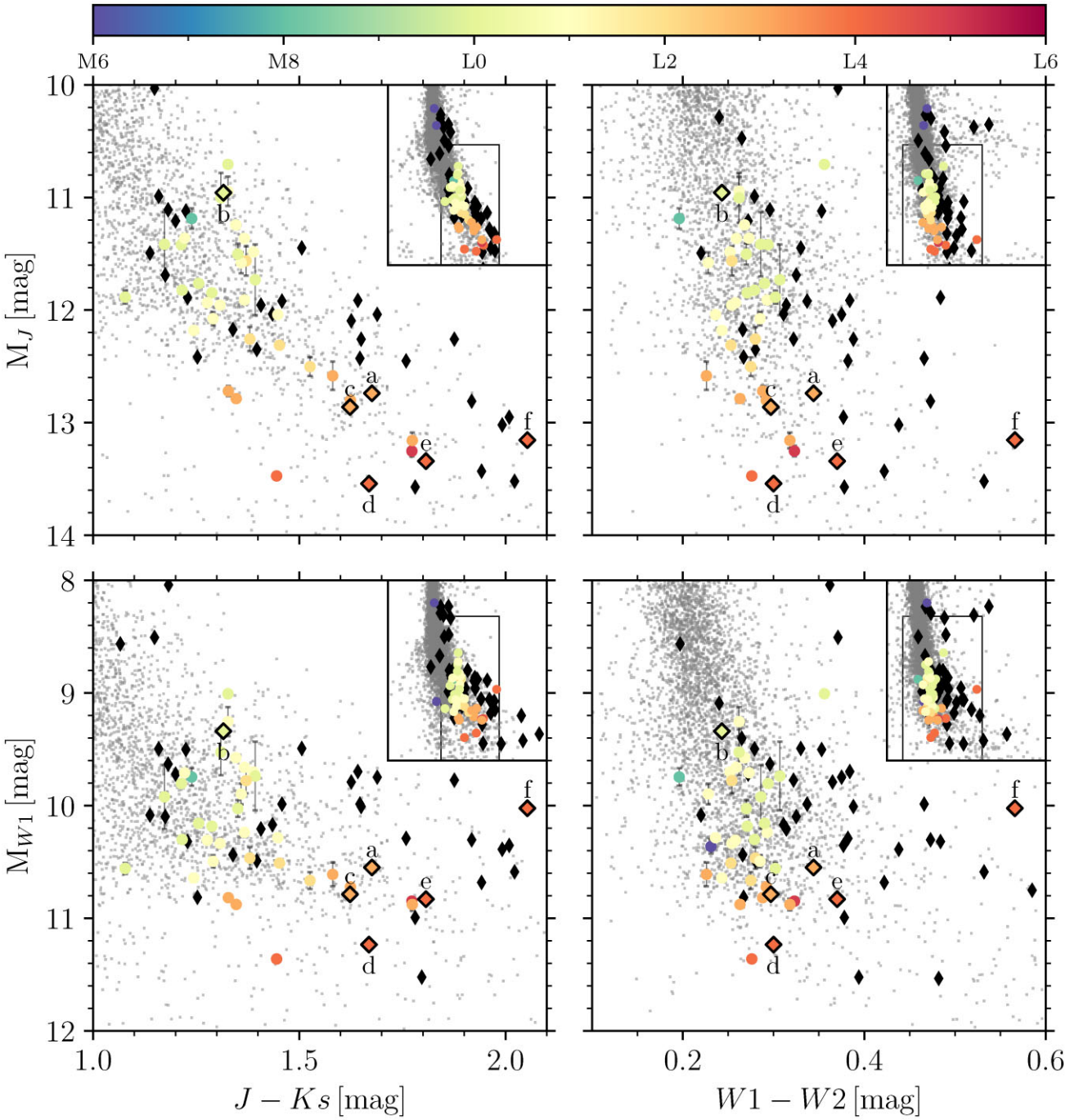

Figure 12. CAMDs of 2MASS and AllWISE photometry, focused on the majority of this sample (an inset of the full sequence is shown in the upper right). The 2MASS $J - K_s$ colour is on the x axis for the first column, with the AllWISE $W1 - W2$ colour on the x axis on the second column. Absolute 2MASS J magnitude is on the y axis for the first row whilst AllWISE M_{W1} is the y axis of the second row. Underlying the plots as grey points is the full UCD sequence from the GUCDS. Known young objects from Faherty et al. (2016) and Liu et al. (2016) are displayed as black diamonds. Each object is coloured by our adopted spectral type, with absolute magnitude error shown. Coloured diamonds are the young candidates discussed in Section Section 5.3.1. Key: a–J0453−1751, b–J0502+1442, c–J1058−1548, d–J1213−0432, e–J1246+4027, f–J1004+5022.

2005). G 124–62 has an RV of $-41.65 \pm 5.91\,\mathrm{km\,s^{-1}}$(Gaia Collaboration 2018a), which is within 1.4σ of the companion (which had large uncertainties).

J1617+7733B: TYC4571-1414-1B is the binary companion of TYC4571-1414-1A (Alonso-Floriano et al. 2015). TYC4571-1414-1A has an RV of $-19 \pm 0.8\,\mathrm{km\,s^{-1}}$ (Gaia Collaboration 2018a), this RV is 0.1σ from the companion RV.

5.2.1 Moving groups

Our results for UVW Galactic kinematic components are presented in Table 5 with each object's moving group classification and associated probability from BANYAN Σ. When accounting for RV in BANYAN Σ, the resultant probability was often lower than the calculation without RV. This was due to the Bayesian probabilities being designed

for a higher recovery rate (moving from 82 per cent to 90 per cent) when accounting for the RV (see the BANYAN Σcautionary note,[8] Gagné et al. 2018). In addition, the RV uncertainties from this work are much higher than proper motion or parallax uncertainties from *Gaia*.

We find four objects are members of the following young moving groups and clusters: Argus (30–50 Myr; Makarov & Urban 2000); β Pictoris (Zuckerman et al. 2001), 20–26 Myr (Mamajek & Bell 2014; Couture, Gagné & Doyon 2023, and references therein); Carina-Near (∼200 Myr; Zuckerman et al. 2006); and the Hyades cluster (600–800 Myr, Perryman et al. 1998; Lodieu, Rebolo & Pérez-Garrido 2018; Martín et al. 2018). These objects (J1058−1548, J0453−1751, J1213−0432, and J0502+1442, respectively) are discussed below in Section 5.3.1.

5.2.2 *Galactic components*

Thin disc objects were differentiated from thick disc and halo objects using the LSR corrected UVW Galactic velocities; the thick disc and halo objects were those with $V_{\rm total} > 70\,{\rm km\,s^{-1}}$ and $V_{\rm total} > 180\,{\rm km\,s^{-1}}$, respectively (Nissen & Schuster 2010). $V_{\rm total}$ is the total space velocity. We calculated upper and lower bounds for UVW Galactic velocities using the propagated parallax, proper motion, and RV errors; these UVW velocities with associated uncertainties are shown in Fig. 10. The objects J1109−1606 ($V_{\rm total} = 103 \pm 5\,{\rm km\,s^{-1}}$) and J1539−0520 ($V_{\rm total} = 69 \pm 4\,{\rm km\,s^{-1}}$) are found using the above criteria to be most likely thick disc objects, and are highlighted in Fig. 10. J1539−0520, is a borderline thick disc object, within 1σ of the thick disc cut-off. Considering that a nearby object is most likely within the thin disc (Holmberg, Nordström & Andersen 2009), J1539−0520 is a reasonable thick disc candidate, hence the inclusion here. It was also assigned a 64.6 per cent probability of being in the thick disc by Cooper et al. (2024), although it did not pass the conservative subdwarf candidate selection criteria in that work. Without metallicity information, an object being in the thick disc is not a direct inference on age. These objects are worth visiting with higher resolution spectroscopy to gain metallicity information, to confirm any potential subdwarf candidacy. This future work would also involved gathering NIR spectra, as in work by Zhang (2018), Zhang et al. (2018), and references therein.

5.3 Astrophysical parameters

We present the $T_{\rm eff}$ and $\log g$ values from the model fitting (Section 4.2) in Table 6 along with $\widehat{T_{\rm eff}}$, assuming our adopted spectral type and equation (4) by Filippazzo et al. (2015) and `teff_espucd` values from *Gaia* DR3. In Fig. 11, we plot the difference between our value and the expected value. In the cases of objects with both R2500I and R300R spectra available, we default to the higher resolution result.

Although the best-fitting surface gravity values can be indicative of youth, they are quite degenerate and without corresponding metallicity values, therefore they are not relied upon in our discussion below. The best-fitting spectral subtypes and BT-Settl models are shown in a spectral sequence for R2500I VPH spectra in Figs A1 and A2.

Fig. 12 shows a set of colour-absolute magnitude diagrams (CAMD), 2MASS $J - K_s$, 2MASS M_J, AllWISE $W1 - W2$, and AllWISE M_{W1}. Parallaxes from *Gaia* were used to generate the absolute magnitudes. Highlighted here are the objects with spectral features that are indicative of youth. These are compared to known young UCDs from Faherty et al. (2016) and Liu et al. (2016, 'VL-G' or 'Young'), as well as the full sample from the GUCDS. These young objects tend to be over-bright, although the effect varies across filters and is further complicated by intrinsic scatter plus variability.

5.3.1 *Individual objects*

We further discuss here objects we have indicated as being non-typical, with interesting features or results. We check for any age classifications, based on the moving group membership from BANYAN Σ and location on the CAMD in Fig. 12. There are additional objects which exist in the same colour space as our highlighted objects in Fig. 12 which are not discussed below. This is because there can be large implicit colour scatter due to unresolved binarity, metallicity, and dust. Hence, only objects which are interesting either spectrally or kinematically are discussed. The following four objects were found to be members of the moving groups listed above, in Section 5.2.1.

J0453−1751: This L3 object, 2MASS J04532647−1751543, is a probable member of β Pictoris with a 99 per cent confidence, this is an increase on the 55 per cent categorization by Ujjwal et al. (2020, using *Gaia* DR2 data). Gagné et al. (2015b) by comparison found this object as a member (96 per cent) of the similarly aged Columba association (20–40 Myr; Torres et al. 2008). We have used *Gaia* DR3 kinematics, which are consistent with the values from *Gaia* DR2 but with reduced uncertainties. In *Gaia* DR2 (Gaia Collaboration 2018a), this was $\varpi = 33.2 \pm 0.6$ mas, $\mu_\alpha \cos\delta = +44.6 \pm 0.7\,{\rm mas\,yr^{-1}}$, and $\mu_\delta = -20.8 \pm 0.8\,{\rm mas\,yr^{-1}}$. In *Gaia* DR3 (Gaia Collaboration 2023), $\varpi = 33.1 \pm 0.5$ mas, $\mu_\alpha \cos\delta = +44.4 \pm 0.4\,{\rm mas\,yr^{-1}}$, and $\mu_\delta = -20.6 \pm 0.4\,{\rm mas\,yr^{-1}}$. The work by Best et al. (2020) is in broad agreement, with larger uncertainties, $\pi = 37.4 \pm 5.7$ mas, $\mu_\alpha \cos\delta = +34.7 \pm 4.9\,{\rm mas\,yr^{-1}}$, and $\mu_\delta = -24.0 \pm 3.9\,{\rm mas\,yr^{-1}}$. The change from *Gaia* DR2 to *Gaia* DR3 in isolation did not alter the confidence (99.2 per cent), whereas the inclusion of our adopted RV value dropped this to 98.9 per cent. Our adopted RV was $15.0 \pm 8.3\,{\rm km\,s^{-1}}$, which is within 1σ of the 'optimal' RV from BANYAN Σ, $21.5 \pm 1.5\,{\rm km\,s^{-1}}$. From Fig. 12, we see J0453−1751 (a) is photometrically similar to known young objects. Its $T_{\rm eff}$ of 1850 ± 70 K is in good agreement with $\widehat{T_{\rm eff}}$ and `teff_espucd`, although is cooler than the 2100 K from Gagné et al. (2015a). We can conclude that this object is an L3 within β Pictoris.

J0502+1442: 2MASS J05021345+1442367, an L0, we find as a member of the Hyades cluster with a 99 per cent probability. This improves the membership confidence by Gagné & Faherty (2018, 75 per cent) and concurs with the classifications by Gaia Collaboration (100 per cent confidence, 2018b); Cantat-Gaudin et al. (100 per cent confidence, 2020, using the Melotte 25 name). Works by Oh & Evans (2020) and Spina et al. (2021) also placed this object in Melotte 25 with 96 per cent and 99 per cent confidences, respectively. It also agrees with the classification by Lodieu et al. (2019), which had a 'c parameter' of 5.88, well within their Hyades membership limit, $c < 25.9$. Fig. 12, places J0502+1442 (b) also as photometrically similar to known young objects, being somewhat over-bright, although there is considerable overlap with standard M-L sequence. With a $T_{\rm eff}$ of 2212 ± 126 K, J0502+1442 is an L0 object in the Hyades cluster.

J1058−1548: Another L3 object, SIPS J1058−1548, is classified with 93 per cent confidence as a member of Argus. Gagné et al. (2015b) had the same classification with a much lower probability (35 per cent). *Gaia* DR2 astrometry in isolation gave a confidence of 96.3 per cent, whilst *Gaia* DR3 reduced this to 94.8 per cent,

[8] http://www.exoplanetes.umontreal.ca/banyan/banyansigma.php

the inclusion of our adopted RV value further dropped this to 93.1 per cent. Our adopted RV was $-0.9 \pm 11.1\,\mathrm{km\,s^{-1}}$, which is within 1σ of the 'optimal' RV from BANYAN Σ, $8.5 \pm 1.4\,\mathrm{km\,s^{-1}}$. Specifically, in *Gaia* DR2, this was $\varpi = 54.6 \pm 0.5$ mas, $\mu_\alpha \cos\delta = -258.1 \pm 0.8\,\mathrm{mas\,yr^{-1}}$, and $\mu_\delta = +31.1 \pm 0.7\,\mathrm{mas\,yr^{-1}}$. In *Gaia* DR3, $\varpi = 55.1 \pm 0.3$ mas, $\mu_\alpha \cos\delta = -258.6 \pm 0.3\,\mathrm{mas\,yr^{-1}}$, and $\mu_\delta = +30.8 \pm 0.3\,\mathrm{mas\,yr^{-1}}$. These values are in broad agreement with non-*Gaia* works, where π ranges from 49.2 mas–66.5 mas, $\mu_\alpha \cos\delta$ from $-60\,\mathrm{mas\,yr^{-1}}(\pm 160\,\mathrm{mas\,yr^{-1}})$ to $-276\,\mathrm{mas\,yr^{-1}}$and μ_δ from $+14\,\mathrm{mas\,yr^{-1}}$to $+210\,\mathrm{mas\,yr^{-1}}(\pm 150\,\mathrm{mas\,yr^{-1}})$; c.f. Dahn et al. (2002); Caballero (2007); Deacon & Hambly (2007); Schmidt et al. (2007); Faherty et al. (2009, 2012); Weinberger et al. (2016); Dahn et al. (2017); Smart et al. (2018). J1058−1548 has a $T_{\rm eff}$=1900 ± 102 K (in exact agreement with Gagné et al. 2015a), but is not as convincingly overbright as neighbouring known young objects, see (c) in Fig. 12. Sanghi et al. (2023) conclude that for J1058−1548, 'it is probable that the YMG assignment [Argus] is incorrect,' because their spectrum well matched L-dwarf FLD-G standards, although the log g value of 4.27 dex was an outlier and more typical of a VL-G object (their fig. 21). The log g value in this work was 5.0 ± 0.3 dex, although this is less robust than that from Sanghi et al. (2023), who also had a much lower $T_{\rm eff}$=1570 K, which itself is more akin to a cooler object, ≈L5. We would argue that this a probable L3 member of Argus but more high resolution spectra and modelling is required to ascertain youth.

J1213−0432: 2MASS J12130336−0432437 (L4) we classify as a member of Carina-Near or Argus (98 per cent), which is an update on the 75 per cent classification of being in Carina-Near by Gagné & Faherty (2018). Just using *Gaia* DR2 astrometry gave a confidence of 68.5 per cent (with a 30.6 per cent likelihood of being in Argus), whilst *Gaia* DR3 increased this to 74.3 per cent (24.7 per cent for Argus), the inclusion of our adopted RV value (with large uncertainty) updated this to 72.0 per cent, with a 26.0 per cent likelihood of being in Argus. Our adopted RV was $-25.3 \pm 22.4\,\mathrm{km\,s^{-1}}$, which is within 1.5σ of the 'optimal' RV from BANYAN Σ, $2.4 \pm 0.8\,\mathrm{km\,s^{-1}}$. In *Gaia* DR2, it was $\varpi = 59.5 \pm 1.0$ mas, $\mu_\alpha \cos\delta = -368.1 \pm 2.2\,\mathrm{mas\,yr^{-1}}$and $\mu_\delta = -34.6 \pm 1.4\,\mathrm{mas\,yr^{-1}}$. In *Gaia* DR3, $\varpi = 59.1 \pm 0.6$ mas, $\mu_\alpha \cos\delta = -367.9 \pm 0.7\,\mathrm{mas\,yr^{-1}}$and $\mu_\delta = -34.0 \pm 0.5\,\mathrm{mas\,yr^{-1}}$. The work by Best et al. (2020) is also in good agreement, $\pi = 56.3 \pm 3.8$ mas, $\mu_\alpha \cos\delta = -380.9 \pm 2.7\,\mathrm{mas\,yr^{-1}}$, and $\mu_\delta = -33.4 \pm 2.4\,\mathrm{mas\,yr^{-1}}$. Fig. 12(d) shows this object as being underbright compared with known young objects, with a $T_{\rm eff}$ of 1783 ± 143 K. Being the age of Carina-Near could explain this relative underbrightness, as it should be tending towards field-like behaviour. This object can be classified then as an L4 member of Carina-Near.

There are two further field objects that we have highlighted as interesting due to their spectral features:

J1246+4027: The L4 dwarf, 2MASSW J1246467+402715, observed at the two resolutions, is of interest due to the potential Li I detection at ≈6708 Å. As this feature is only in the wavelength regime of the R300R spectra, this is not definitive enough a detection to confirm lithium [see discussion by Martín et al. 2018, using the equation from Cayrel (1988)]. Higher resolution ($R \gtrsim 2000$) spectra would be required for confirmation (Gálvez-Ortiz et al. 2014). Assuming a true detection, employing the lithium test (Rebolo, Martin & Magazzu 1992) alongside our fitted effective temperature of $T_{\rm eff} = 1750 \pm 91$ K would identify this object as being substellar. This $T_{\rm eff}$ is in good agreement with the expected temperature of $\widehat{T_{\rm eff}} = 1717 \pm 116$ K and the *Gaia* DR3 $T_{\rm eff}$ of 1780 ± 162 K. This substellar argument is in line with discussion by Basri (1998), Martín, Basri & Zapatero Osorio (1999a), and Kirkpatrick et al. (1999), because our $T_{\rm eff}$ is in the range $2670 > T_{\rm eff} > 1400$ K. Fig. 12 suggests J1246+4027 (e) neighbours some known young objects. The best-fitting model had a surface gravity of $\log g = 4.6 \pm 0.3$ dex, although we have no complementary metallicity information. BANYAN Σ finds no correlation with any known young moving groups. J1246+4027 could be classed as an L4β field object.

J1004+5022: G 196–3B is known to be a low gravity brown dwarf (Rebolo et al. 1998; Kirkpatrick et al. 2008; Allers & Liu 2013), to which we concur, with a spectral subtype of L3β. Our log g value is 4.5 ± 0.2 dex ($T_{\rm eff} = 1740 \pm 113$ K), as would be expected from the already known young nature. This object sits extremely red and over-bright in Fig. 12(f), even more extremely than most known young objects. It is a companion to the well known G 196–3A M3 star, to which we compared our kinematics in Section 5.2, finding a 0.1σ difference. There is much deeper discussion on this benchmark system by Zapatero Osorio et al. (2010), which measures an angular separation of $\rho = 15.99 \pm 0.06$arcsec. Combined with a *Gaia* DR3 parallax of $\varpi = 46.1952 \pm 0.5452$ mas (in agreement with the 49.0 ± 2.3 mas and 41.0 ± 4.1 mas measurements by Zapatero Osorio et al. 2014; Liu et al. 2016, respectively), this implies a projected separation of $s = 739 \pm 1$ AU. This is slightly more than the projected physical separation range calculated by Zapatero Osorio et al. (2010), 285–640 AU. We found a probability of the secondary being a field object of 99.9 per cent, which is an increase on the 32 per cent probability of being a member of AB Doradus by Gagné et al. (2014). Liu et al. (2016) kinematically confirmed that G 196–3B is a young field object. This is also in agreement with the 50 per cent classification of the primary being a member of AB Doradus by Schlieder et al. (2012a), which was later downgraded to 0 per cent by Binks & Jeffries (2016); however, the primary was also classified as being a member of the controvertible Castor moving group (Barrado y Navascues 1998) with 75 per cent confidence (Klutsch et al. 2014). The Castor moving group was not included in BANYAN Σ, hence not being included in our analysis. We classify this object as an L3β object.

6 SUMMARY AND CONCLUSIONS

We have presented the low and mid resolution optical GTC/OSIRIS spectra of 53 objects observed between 2015 and 2016. Our data reduction was non-standard, using a pipeline package, `PYPEIT`; this reduction was validated with an independent `IRAF` spectral extraction and calibration for one of the objects. We used `KASTREDUX` to create 53 automated spectral types, six of which are for objects not yet spectrally typed, alongside the established technique of comparing against spectral standard template spectra. We found that our chosen spectral reduction package, `PYPEIT`, introduced some non-optimal artefacts during reduction. One example is a spike appearing near the O_2 A band from the telluric correction procedure, which required interpolating over for visualization purposes (it does not affect wavelength solutions).

In addition to using new data reduction software, we also used novel analysis software, `RVFITTER`, that we developed to perform manual line centring and cross-correlation (against BT-Settl CIFIST models). The `RVFITTER` code also used an uncertainty-weighted mean to create an adopted RV. This produced 46 RVs, 29 of which are new, which we have validated against standard `IRAF` and `IDL` software techniques. There were 17 RVs which were compared against literature values, showing good agreement with a median difference of $7.8\,\mathrm{km\,s^{-1}}$, adopted as our systematic uncertainty. Our median RV uncertainty was $11.2\,\mathrm{km\,s^{-1}}$, indicating that further high-

resolution spectroscopy would be necessary to validate our RV values and conclusions. The cross-correlation also produced mean $T_{\rm eff}$ and log g values for all 53 objects.

In this work, we performed further analysis on our spectral types, RVs, and $T_{\rm eff}$ values by making comparisons to the literature where appropriate and ensuring all results were within two spectral subtypes, $\Delta{\rm RV} < 2\sigma$ and $\Delta T_{\rm eff} < 2\sigma$ (against $\widehat{T_{\rm eff}}$ and *Gaia* DR3 `teff_espucd`). We then discussed any measurements which did not conform with these standards, such as J0940+2946, which had a $\Delta{\rm RV} = 2.69\sigma$. There were four objects that we classified through BANYAN Σ as being a member of a young moving group: SIPS J1058-1548 (J1058−1548), 2MASS J04532647-1751543 (J0453−1751), 2MASS J12130336-0432437 (J1213−0432), and 2MASS J05021345+1442367 (J0502+1442). There were two objects we placed as members of the thick disc: SIPS J1109-1606 (J1109−1606) and 2MASS J15394189-0520428 (J1539−0520).

Finally, by relating to gravity sensitive alkali lines and the aforementioned young moving group members, we discuss the interesting young candidates J1246+4027 and J1004+5022. 2MASSW J1246467+402715 (J1246+4027) has a potential lithium indication and is otherwise an L4β field object. G 196–3B (J1004+5022) is confirmed as a young object, as was known from its primary companion.

In conclusion, this work was part of the GUCDS series of papers. A search of the GUCDS yields 145 known L dwarfs with measured RVs, excluding those from the SDSS. The 29 new L dwarf RVs presented in this work are therefore an ≈20 per cent increase to the number of 6D complete L dwarfs. A number of interesting objects were identified or confirmed, either into young moving groups or young field objects. We used novel open-source techniques at all stages of our procedure, which we make available to the astronomical community. These techniques have been compared with established and accepted techniques in order to generate a baseline of trust. The observation campaign to complete the 30 pc sample is ongoing, with predominantly NIR spectrographs. This campaign will continue to produce work discussing, expanding, and exploring this 30 pc sample.

DATA AVAILABILITY

The data underlying this article will be available in CDS VizieR,[9] the GUCDS Data Browser,[10] and the SIMPLE Database.[11] The code used to generate the reduced spectra and analysis is available either through open-source repositories (see Cooper 2022b, and the acknowledgements) or upon any reasonable request.

FUNDING

WJC is funded by a University of Hertfordshire studentship. WJC, HRAJ, SF, BB, and DJP recognize the computing infrastructure provided via STFC grant ST/R000905/1 at the University of Hertfordshire. RLS has been supported by a STSM grant from COST Action CA18104: MW-Gaia. Funded in part by Chinese Academy of Sciences President's International Fellowship Initiative, Grant No. 2020VMA0033. DM, JAC, MCGO, and NL acknowledge financial support from the Spanish Agencia Estatal de Investigación of the Ministerio de Ciencia e Innovación (AEI/10.13039/501100011033) and the ERDF 'A way of making Europe' through projects PID2019-109522GB-C51, -53, and -54 and PID2022-137241NB-C41, -42, and -44.

ACKNOWLEDGEMENTS

We would like to thank the anonymous referees for their very useful and much appreciated feedback, which has much improved the manuscript. Based on observations made with the Gran Telescopio Canarias (GTC), installed in the Spanish Observatorio del Roque de los Muchachos of the Instituto de Astrofísica de Canarias, on the island of La Palma. This work is based on data obtained with the instrument OSIRIS, built by a Consortium led by the Instituto de Astrofísica de Canarias in collaboration with the Instituto de Astronomía of the Universidad Autónoma de México. OSIRIS was funded by GRANTECAN and the National Plan of Astronomy and Astrophysics of the Spanish Government.

This research has made use of the SIMBAD data base, operated at CDS, Strasbourg, France. This work presents results from the European Space Agency (ESA) space mission *Gaia*. *Gaia*'s data are processed by the Gaia Data Processing and Analysis Consortium (DPAC). Funding for the DPAC is provided by national institutions, in particular the institutions participating in the Gaia Multi Lateral Agreement (MLA). This publication makes use of data products from the Two Micron All Sky Survey, which is a joint project of the University of Massachusetts and the Infrared Processing and Analysis Center/California Institute of Technology, funded by the National Aeronautics and Space Administration and the National Science Foundation. This publication makes use of data products from the Wide-field Infrared Survey Explorer, which is a joint project of the University of California, Los Angeles, and the Jet Propulsion Laboratory/California Institute of Technology, and NEOWISE, which is a project of the Jet Propulsion Laboratory/California Institute of Technology. WISE and NEOWISE are funded by the National Aeronautics and Space Administration.

IRAF is distributed by the National Optical Astronomy Observatory, which is operated by the Association of Universities for Research in Astronomy (AURA) under a cooperative agreement with the National Science Foundation. We have made use of the on-line resources available from the `IDL` Astronomy Library hosted by the NASA Goddard Space Flight Center, in particular the `DEFRINGEFLAT.PRO` routine. We acknowledge the relevant open source packages used in our `PYTHON` (van Rossum & de Boer 1991) codes: `ASTROPY` (Astropy Collaboration 2013, 2018), `BARYCORRPY` (Kanodia & Wright 2018), `KASTREDUX` (Burgasser 2021), `MATPLOTLIB` (Hunter 2007), `NUMPY` (Harris et al. 2020), `PANDAS` (Wes McKinney 2010; pandas development team 2020), `SCIPY` (Virtanen et al. 2020), `SPECUTILS` (Earl et al. 2021), `SPLAT` (Burgasser & Splat Development Team 2017), and `TQDM` (da Costa-Luis et al. 2021). This research also made use of `PYPEIT` (v.1.4.0),[12] a `PYTHON` package for semi-automated reduction of astronomical slit-based spectroscopy (Prochaska et al. 2020a, 2020b).

REFERENCES

Abazajian K. N. et al., 2009, ApJS, 182, 543
Allard F., Homeier D., Freytag B., 2011, in Johns-Krull C., Browning M. K., West A. A., eds, ASP Conf. Ser. Vol. 448, 16th Cambridge Workshop on

[9] https://vizier.cds.unistra.fr/viz-bin/VizieR
[10] https://gucds.inaf.it
[11] https://simple-bd-archive.org/
[12] https://pypeit.readthedocs.io/en/latest/

Cool Stars, Stellar Systems, and the Sun. Astron. Soc. Pac., San Francisco, p. 91
Allers K. N., Liu M. C., 2013, ApJ, 772, 79
Alonso-Floriano F. J., Caballero J. A., Cortés-Contreras M., Solano E., Montes D., 2015, A&A, 583, A85
Andrei A. H. et al., 2011, AJ, 141, 54
Astropy Collaboration A&A, 558, A33
Astropy Collaboration 2018, AJ, 156, 123
Baraffe I., Chabrier G., Allard F., Hauschildt P. H., 1997, A&A, 327, 1054
Baraffe I., Homeier D., Allard F., Chabrier G., 2015, A&A, 577, A42
Bardalez Gagliuffi D. C. et al., 2014, ApJ, 794, 143
Barrado y Navascues D., 1998, A&A, 339, 831
Basri G., 1998, in Rebolo R., Martin E. L., Zapatero Osorio M. R., eds, ASP Conf. Ser. Vol. 134, Brown Dwarfs and Extrasolar Planets. Astron. Soc. Pac., San Francisco, p. 394
Bensby T., Feltzing S., Lundström I., Ilyin I., 2005, A&A, 433, 185
Bergeron P., Leggett S. K., Ruiz M. T., 2001, ApJS, 133, 413
Best W. M. J. et al., 2018, ApJS, 234, 1
Best W. M. J., Liu M. C., Magnier E. A., Dupuy T. J., 2020, AJ, 159, 257
Best W. M. J., Liu M. C., Magnier E. A., Dupuy T. J., 2021, AJ, 161, 42
Binks A. S., Jeffries R. D., 2016, MNRAS, 455, 3345
Blake C. H., Charbonneau D., White R. J., 2010, ApJ, 723, 684
Blouin S., Dufour P., Allard N. F., 2018, ApJ, 863, 184
Bochanski J. J., West A. A., Hawley S. L., Covey K. R., 2007, AJ, 133, 531
Bohlin R. C., Colina L., Finley D. S., 1995, AJ, 110, 1316
Bohlin R. C., Gordon K. D., Tremblay P. E., 2014, PASP, 126, 711
Bouy H., Brandner W., Martín E. L., Delfosse X., Allard F., Basri G., 2003, AJ, 126, 1526
Burgasser A., 2021, kastredux. Available at: https://github.com/aburgasser/kastredux
Burgasser A. J., Splat Development Team, 2017, Astronomical Society of India Conference Series, 7
Burgasser A. J. et al., 2002, ApJ, 564, 421
Burgasser A. J., Cruz K. L., Kirkpatrick J. D., 2007, ApJ, 657, 494
Burgasser A. J. et al., 2015, ApJS, 220, 18
Burningham B. et al., 2013, MNRAS, 433, 457
Burningham B., Marley M. S., Line M. R., Lupu R., Visscher C., Morley C. V., Saumon D., Freedman R., 2017, MNRAS, 470, 1177
Burrows A. et al., 1997, ApJ, 491, 856
Caballero J. A., 2007, ApJ, 667, 520
Caballero J. A., 2009, A&A, 507, 251
Calamari E. et al., 2022, ApJ, 940, 164
Cantat-Gaudin T. et al., 2020, A&A, 640, A1
Carrasco J. M. et al., 2021, A&A, 652, A86
Cayrel R., 1988, in Cayrel de Strobel G., Spite M., eds, Proc. IAU Symp. 132, The Impact of Very High S/N Spectroscopy on Stellar Physics. Springer, Dordrecht, p. 345
Cepa J., 1998, Ap&SS, 263, 369
Chabrier G., 2003, PASP, 115, 763
Chabrier G., Baraffe I., 1997, A&A, 327, 1039
Chabrier G., Baraffe I., Allard F., Hauschildt P., 2000, ApJ, 542, L119
Chambers K. C. et al., 2016, preprint (arXiv:1612.05560)
Coşkunoğlu B. et al., 2011, MNRAS, 412, 1237
Cooper W. J., 2022a, gaiaxpy-batch. Available at: https://doi.org/10.5281/zenodo.6653446
Cooper W. J., 2022b, rvfitter. Available at: https://doi.org/10.5281/zenodo.6984399
Cooper W. J., Smart R. L., Jones H. R. A., Sarro L. M., 2024, MNRAS, 527, 1521
da Costa-Luis C. et al., 2021, tqdm: A fast, Extensible Progress Bar for Python and CLI. Available at: https://doi.org/10.5281/zenodo.5517697
Couture D., Gagné J., Doyon R., 2023, ApJ, 946, 6
Creevey O. L. et al., 2023, A&A, 674, A26
Crifo F., Phan-Bao N., Delfosse X., Forveille T., Guibert J., Martín E. L., Reylé C., 2005, A&A, 441, 653
Cruz K. L., Reid I. N., Liebert J., Kirkpatrick J. D., Lowrance P. J., 2003, AJ, 126, 2421
Cruz K. L. et al., 2007, AJ, 133, 439
Cruz K. L., Kirkpatrick J. D., Burgasser A. J., 2009, AJ, 137, 3345
Cutri R. M. et al., 2003, VizieR Online Data Catalog, p. II/246
Czekaj M. A., Robin A. C., Figueras F., Luri X., Haywood M., 2014, A&A, 564, A102
Dahn C. C. et al., 2002, AJ, 124, 1170
Dahn C. C. et al., 2017, AJ, 154, 147
De Angeli F. et al., 2023, A&A, 674, A2
Deacon N. R., Hambly N. C., 2007, A&A, 468, 163
Delfosse X., Forveille T., Beuzit J. L., Udry S., Mayor M., Perrier C., 1999, A&A, 344, 897
van Dokkum P. G., 2001, PASP, 113, 1420
Dupuy T. J., Liu M. C., 2012, ApJS, 201, 19
Dupuy T. J., Liu M. C., Ireland M. J., 2009, ApJ, 692, 729
Earl N. et al., 2021, astropy/specutils: V1.5.0. Available at: https://doi.org/10.5281/zenodo.5721652
Edlen B., 1953, J. Opt. Soc. Am., 43, 339
Epchtein N. et al., 1997, The Messenger, 87, 27
Faherty J. K., Burgasser A. J., Cruz K. L., Shara M. M., Walter F. M., Gelino C. R., 2009, AJ, 137, 1
Faherty J. K. et al., 2012, ApJ, 752, 56
Faherty J. K. et al., 2016, ApJS, 225, 10
Filippazzo J. C., Rice E. L., Faherty J., Cruz K. L., Van Gordon M. M., Looper D. L., 2015, ApJ, 810, 158
Gagné J., Faherty J. K., 2018, ApJ, 862, 138
Gagné J., Lafrenière D., Doyon R., Malo L., Artigau É., 2014, ApJ, 783, 121
Gagné J. et al., 2015a, ApJS, 219, 33
Gagné J., Lafrenière D., Doyon R., Malo L., Artigau É., 2015b, ApJ, 798, 73
Gagné J. et al., 2018, ApJ, 856, 23
Gaia Collaboration 2016, A&A, 595, A1
Gaia Collaboration 2018a, A&A, 616, A1
Gaia Collaboration 2018b, A&A, 616, A10
Gaia Collaboration 2021a, A&A, 649, A1
Gaia Collaboration 2021b, A&A, 649, A6
Gaia Collaboration 2023, A&A, 674, A1
Gálvez-Ortiz M. C. et al., 2014, MNRAS, 439, 3890
Geballe T. R. et al., 2002, ApJ, 564, 466
Gliese W., 1957, Astron. Rechen-Inst. Heidelberg Mitt. Ser. A, 8, 1
Golovin A., Reffert S., Just A., Jordan S., Vani A., Jahreiß H., 2023, A&A, 670, A19
Hambly N. C. et al., 2001, MNRAS, 326, 1279
Hamuy M., Walker A. R., Suntzeff N. B., Gigoux P., Heathcote S. R., Phillips M. M., 1992, PASP, 104, 533
Hamuy M., Suntzeff N. B., Heathcote S. R., Walker A. R., Gigoux P., Phillips M. M., 1994, PASP, 106, 566
Harris C. R. et al., 2020, Nature, 585, 357
Hawley S. L. et al., 2002, AJ, 123, 3409
Henry T. J., Kirkpatrick J. D., Simons D. A., 1994, AJ, 108, 1437
Holmberg J., Nordström B., Andersen J., 2009, A&A, 501, 941
Horne K., 1986, PASP, 98, 609
Hsu C.-C. et al., 2021, ApJS, 257, 45
Hunter J. D., 2007, Comput. Sci. Eng., 9, 90
Johnson D. R. H., Soderblom D. R., 1987, AJ, 93, 864
Kanodia S., Wright J., 2018, Res. Notes Am. Astron. Soc., 2, 4
Karalidi T., Marley M., Fortney J. J., Morley C., Saumon D., Lupu R., Visscher C., Freedman R., 2021, ApJ, 923, 269
Katz D. et al., 2023, A&A, 674, A5
Kendall T. R., Mauron N., Azzopardi M., Gigoyan K., 2003, A&A, 403, 929
Kendall T. R., Delfosse X., Martín E. L., Forveille T., 2004, A&A, 416, L17
Kendall T. R. et al., 2007, A&A, 466, 1059
Kesseli A. Y., West A. A., Veyette M., Harrison B., Feldman D., Bochanski J. J., 2017, ApJS, 230, 16
Kiman R., Schmidt S. J., Angus R., Cruz K. L., Faherty J. K., Rice E., 2019, AJ, 157, 231
Kirkpatrick J. D., 2005, ARA&A, 43, 195
Kirkpatrick J. D. et al., 1999, ApJ, 519, 802
Kirkpatrick J. D. et al., 2000, AJ, 120, 447
Kirkpatrick J. D. et al., 2008, ApJ, 689, 1295
Kirkpatrick J. D. et al., 2010, ApJS, 190, 100

Kirkpatrick J. D. et al., 2021, ApJS, 253, 7
Klutsch A., Freire Ferrero R., Guillout P., Frasca A., Marilli E., Montes D., 2014, A&A, 567, A52
Knapp G. R. et al., 2004, AJ, 127, 3553
Kramida A., Ralchenko Y., Reader J., and NIST ASD Team, 2021, NIST Atomic Spectra Database (version 5.9)., https://physics.nist.gov/asd
Kroupa P., 2001, MNRAS, 322, 231
Lagarde N. et al., 2021, A&A, 654, A13
Landsman W. B., 1993, in Hanisch R. J., Brissenden R. J. V., Barnes J., eds, ASP Conf. Ser. Vol. 52, Astronomical Data Analysis Software and Systems II. Astron. Soc. Pac., San Francisco, p. 246
Lawrence A. et al., 2007, MNRAS, 379, 1599
Leggett S. K. et al., 2002, ApJ, 564, 452
Liu M. C., Dupuy T. J., Allers K. N., 2016, ApJ, 833, 96
Lodieu N., Scholz R. D., McCaughrean M. J., Ibata R., Irwin M., Zinnecker H., 2005, A&A, 440, 1061
Lodieu N., Deacon N. R., Hambly N. C., 2012, VizieR Online Data Catalog, p. J/MNRAS/422/1495
Lodieu N., Espinoza Contreras M., Zapatero Osorio M. R., Solano E., Aberasturi M., Martín E. L., Rodrigo C., 2017, A&A, 598, A92
Lodieu N., Rebolo R., Pérez-Garrido A., 2018, A&A, 615, L12
Lodieu N., Smart R. L., Pérez-Garrido A., Silvotti R., 2019, A&A, 623, A35
Lucas P. W., Roche P. F., 2000, MNRAS, 314, 858
Makarov V. V., Urban S., 2000, MNRAS, 317, 289
Mamajek E. E., Bell C. P. M., 2014, MNRAS, 445, 2169
Marley M. S., Seager S., Saumon D., Lodders K., Ackerman A. S., Freedman R. S., Fan X., 2002, ApJ, 568, 335
Marley M. S. et al., 2021, ApJ, 920, 85
Marocco F. et al., 2013, AJ, 146, 161
Marocco F. et al., 2017, MNRAS, 470, 4885
Marocco F. et al., 2020, MNRAS, 494, 4891
Marocco F. et al., 2021, ApJS, 253, 8
Martín E. L., Basri G., Zapatero Osorio M. R., 1999a, AJ, 118, 1005
Martín E. L., Delfosse X., Basri G., Goldman B., Forveille T., Zapatero Osorio M. R., 1999b, AJ, 118, 2466
Martín E. L. et al., 2010, A&A, 517, A53
Martín E. L., Lodieu N., Pavlenko Y., Béjar V. J. S., 2018, ApJ, 856, 40
McCleery J. et al., 2020, MNRAS, 499, 1890
McKinney W., 2010, in van de Walt S., Millman J. eds, Data Structures for Statistical Computing in Python, Proceedings of the 9th Python in Science Conference,SciPy. p. 56
McMahon R. G., Banerji M., Gonzalez E., Koposov S. E., Bejar V. J., Lodieu N., Rebolo R., VHS Collaboration, 2021, VizieR Online Data Catalog, p. II/367
Meisner A. M., Caselden D., Schlafly E. F., Kiwy F., 2023, AJ, 165, 36
Minniti D. et al., 2010, New Astron., 15, 433
Montegriffo P. et al., 2023, A&A, 674, A3
Nissen P. E., Schuster W. J., 2010, A&A, 511, L10
Oh S., Evans N. W., 2020, MNRAS, 498, 1920
Oke J. B., 1974, ApJS, 27, 21
Oke J. B., 1990, AJ, 99, 1621
pandas development team T., 2020, pandas-dev/pandas: Pandas. Available at: https://doi.org/10.5281/zenodo.3509134
Perryman M. A. C. et al., 1998, A&A, 331, 81
Phan-Bao N. et al., 2008, MNRAS, 383, 831
Phan-Bao N., Lee C.-F., Ho P. T. P., Tang Y.-W., 2011, ApJ, 735, 14
Pinfield D. J., Hodgkin S. T., Jameson R. F., Cossburn M. R., Hambly N. C., Devereux N., 2000, MNRAS, 313, 347
Pinfield D. J., Jones H. R. A., Lucas P. W., Kendall T. R., Folkes S. L., Day-Jones A. C., Chappelle R. J., Steele I. A., 2006, MNRAS, 368, 1281
Prochaska J. X. et al., 2020a, pypeit/PypeIt: Release 1.0.0
Prochaska J. X. et al., 2020b, J. Open Source Softw., 5, 2308
Rebolo R., Martin E. L., Magazzu A., 1992, ApJ, 389, L83
Rebolo R., Zapatero Osorio M. R., Madruga S., Bejar V. J. S., Arribas S., Licandro J., 1998, Science, 282, 1309
Reid I. N., Cruz K. L., Kirkpatrick J. D., Allen P. R., Mungall F., Liebert J., Lowrance P., Sweet A., 2008, AJ, 136, 1290
Reiners A., Homeier D., Hauschildt P. H., Allard F., 2007, A&A, 473, 245
Reylé C., Jardine K., Fouqué P., Caballero J. A., Smart R. L., Sozzetti A., 2021, A&A, 650, A201
Riedel A. R., Blunt S. C., Lambrides E. L., Rice E. L., Cruz K. L., Faherty J. K., 2017, AJ, 153, 95
Riello M. et al., 2021, A&A, 649, A3
Robert J. et al., 2016, ApJ, 830, 144
Rojo P. M., Harrington J., 2006, ApJ, 649, 553
van Rossum G., de Boer J., 1991, CWI Quart.., 4, 283
Ruz-Mieres D., 2022, gaia-dpci/GaiaXPy: GaiaXPy 1.1.4. Available at: https://doi.org/10.5281/zenodo.6674521
Salpeter E. E., 1955, ApJ, 121, 161
Sanghi A. et al., 2023, ApJ, 959, 63
Sarro L. M. et al., 2023, A&A, 669, A139
Saumon D., Marley M. S., 2008, ApJ, 689, 1327
Saumon D., Hubbard W. B., Burrows A., Guillot T., Lunine J. I., Chabrier G., 1996, ApJ, 460, 993
Scalo J. M., 1986, Fund. Cosmic Phys., 11, 1
Schiavon R. P., Barbuy B., Rossi S. C. F., Milone A., 1997a, ApJ, 479, 902
Schiavon R. P., Barbuy B., Singh P. D., 1997b, ApJ, 484, 499
Schlafly E. F., Meisner A. M., Green G. M., 2019, ApJS, 240, 30
Schlieder J. E., Lépine S., Simon M., 2012a, AJ, 143, 80
Schlieder J. E., Lépine S., Simon M., 2012b, AJ, 144, 109
Schmidt S. J., Cruz K. L., Bongiorno B. J., Liebert J., Reid I. N., 2007, AJ, 133, 2258
Schmidt S. J., West A. A., Hawley S. L., Pineda J. S., 2010, AJ, 139, 1808
Schneider A. C., Cushing M. C., Kirkpatrick J. D., Mace G. N., Gelino C. R., Faherty J. K., Fajardo-Acosta S., Sheppard S. S., 2014, AJ, 147, 34
Seifahrt A., Guenther E., Neuhäuser R., 2005, A&A, 440, 967
Shkolnik E. L., Anglada-Escudé G., Liu M. C., Bowler B. P., Weinberger A. J., Boss A. P., Reid I. N., Tamura M., 2012, ApJ, 758, 56
Skrutskie M. F. et al., 2006, AJ, 131, 1163
Smart R. L., Marocco F., Caballero J. A., Jones H. R. A., Barrado D., Beamín J. C., Pinfield D. J., Sarro L. M., 2017, MNRAS, 469, 401
Smart R. L. et al., 2018, MNRAS, 481, 3548
Smart R. L., Marocco F., Sarro L. M., Barrado D., Beamín J. C., Caballero J. A., Jones H. R. A., 2019, MNRAS, 485, 4423
Smette A. et al., 2015, A&A, 576, A77
Smith L., Lucas P. W., Burningham B., Jones H. R. A., Smart R. L., Andrei A. H., Catalán S., Pinfield D. J., 2014, MNRAS, 437, 3603
Smith L. C. et al., 2018, MNRAS, 474, 1826
Spina L. et al., 2021, MNRAS, 503, 3279
Steele I. A., Jameson R. F., 1995, MNRAS, 272, 630
Stephens D. C., Leggett S. K., 2004, PASP, 116, 9
Stephens D. C. et al., 2009, ApJ, 702, 154
Tinney C. G., Reid I. N., 1998, MNRAS, 301, 1031
Torres C. A. O., Quast G. R., Melo C. H. F., Sterzik M. F., 2008, in Reipurth B., ed., Handbook of Star Forming Regions, Volume II (monograph 5). Astron. Soc. Pac., San Francisco, p. 757
Tremblay P. E., Bergeron P., Gianninas A., 2011, ApJ, 730, 128
Ujjwal K., Kartha S. S., Mathew B., Manoj P., Narang M., 2020, AJ, 159, 166
Virtanen P. et al., 2020, Nat. Methods, 17, 261
Vrba F. J. et al., 2004, AJ, 127, 2948
Vrijmoet E. H., Tokovinin A., Henry T. J., Winters J. G., Horch E., Jao W.-C., 2022, AJ, 163, 178
Weinberger A. J., Boss A. P., Keiser S. A., Anglada-Escudé G., Thompson I. B., Burley G., 2016, AJ, 152, 24
Wenger M. et al., 2000, A&AS, 143, 9
West A. A. et al., 2011, AJ, 141, 97

Wright E. L. et al., 2010, AJ, 140, 1868
York D. G. et al., 2000, AJ, 120, 1579
Zapatero Osorio M. R., Béjar V. J. S., Martín E. L., Rebolo R., Barrado y Navascués D., Bailer-Jones C. A. L., Mundt R., 2000, Science, 290, 103
Zapatero Osorio M. R., Rebolo R., Bihain G., Béjar V. J. S., Caballero J. A., Álvarez C., 2010, ApJ, 715, 1408
Zapatero Osorio M. R., Béjar V. J. S., Miles-Páez P. A., Peña Ramírez K., Rebolo R., Pallé E., 2014, A&A, 568, A6
Zechmeister M. et al., 2019, A&A, 627, A49
Zhang Z., 2018, in 20th Cambridge Workshop on Cool Stars, Stellar Systems and the Sun. p. 44
Zhang Z. H. et al., 2017, MNRAS, 464, 3040
Zhang Z. H. et al., 2018, MNRAS, 480, 5447
Zuckerman B., Song I., Bessell M. S., Webb R. A., 2001, ApJ, 562, L87
Zuckerman B., Bessell M. S., Song I., Kim S., 2006, ApJ, 649, L115

APPENDIX A: ADDITIONAL INFORMATION

A1 Appendix tables

Table A1. Additional information for all observations carried out as part of the two programmes presented here. Note, multiple objects were observed multiple times, with either the same grism or the other. Seeing is given as a range corresponding to reverse wavelength, and is corrected for airmass.

Object Full name	Object short name	Resolution Grism/ VPH	Programme ID	UT Date yyyy-mm-dd	Airmass (z)	Humidity (per cent)	Seeing $\lambda_{max} - \lambda_{min}$
2MASS J00285545−1927165	J0028−1927	R2500I	GTC8-15ITP	2015-08-30	1.54	27	0.90–0.96
2MASS J02354756−0849198	J0235−0849	R2500I	GTC8-15ITP	2015-08-31	1.49	30	0.89–0.94
2MASS J04285096−2253227	J0428−2253	R2500I	GTC8-15ITP	2015-08-31	1.82	32	1.12–1.19
2MASS J04532647−1751543	J0453−1751	R2500I	GTC8-15ITP	2015-10-01	1.51	11	0.67–0.71
2MASS J05021345+1442367	J0502+1442	R2500I	GTC8-15ITP	2015-09-29	1.04	13	0.71–0.76
2MASSI J0605019−234226	J0605−2342	R2500I	GTC8-15ITP	2015-11-30	1.66	58	1.77–1.88
2MASS J07410440+2316377	J0741+2316	R2500I	GTC8-15ITP	2015-12-31	1.05	6	0.90–0.95
SDSS J075259.48+413646.8	J0752+4136	R2500I	GTC8-15ITP	2015-11-28	1.04	17	0.98–1.04
ULAS J080910.65+231515.7	J0809+2315	R2500I	GTC8-15ITP	2015-12-31	1.10	7	1.20–1.27
2MASS J08230316+0240426	J0823+0240	R2500I	GTC8-15ITP	2015-12-31	1.12	7	0.84–0.89
2MASS J08230838+6125208	J0823+6125	R2500I	GTC8-15ITP	2015-11-30	1.21	51	1.27–1.35
2MASS J08472872−1532372	J0847−1532	R300R	GTC54-15A	2015-04-04	1.40	13	1.49–1.73
2MASSW J0918382+213406	J0918+2134	R2500I	GTC8-15ITP	2015-11-30	1.03	52	0.98–1.04
2MASS J09352803−2934596	J0935−2934	R2500I	GTC8-15ITP	2015-11-30	1.90	47	1.79–1.90
2MASS J09385888+0443438	J0938+0443	R2500I	GTC8-15ITP	2015-12-31	1.18	7	0.67–0.72
2MASS J09404793+2946534	J0940+2946	R2500I	GTC8-15ITP	2016-02-26	1.27	13	1.01–1.07
2MASSI J0953212−101420	J0953−1014	R2500I	GTC54-15A	2015-03-31	1.37	16	1.26–1.34
G196−3B	J1004+5022	R2500I	GTC54-15A	2015-04-27	1.09	2	0.83–0.88
G196−3B	J1004+5022	R300R	GTC54-15A	2015-04-27	1.08	2	0.82–0.95
2MASS J10044030−1318186	J1004−1318	R2500I	GTC8-15ITP	2015-12-31	1.36	8	1.26–1.34
DENIS J104731.1−181558	J1047−1815	R300R	GTC54-15A	2015-04-27	1.50	2	1.33–1.54
DENIS J104731.1−181558	J1047−1815	R2500I	GTC54-15A	2015-04-27	1.55	2	1.36–1.44
DENIS J1058.7−1548	J1058−1548	R300R	GTC54-15A	2015-04-27	1.52	2	1.12–1.29
DENIS J1058.7−1548	J1058−1548	R2500I	GTC54-15A	2015-04-27	1.61	1	1.16–1.23
2MASS J11092745−1606515	J1109−1606	R2500I	GTC8-15ITP	2015-12-30	1.42	21	1.18–1.26
2MASS J11270661+4705481	J1127+4705	R2500I	GTC8-15ITP	2015-12-30	1.05	21	0.63–0.67
2MASS J12130336−0432437	J1213−0432	R2500I	GTC54-15A	2015-04-28	1.29	2	0.81–0.86
2MASS J12164560+4927452	J1216+4927	R2500I	GTC8-15ITP	2015-12-31	1.07	8	0.73–0.77
2MASS J12212770+0257198	J1221+0257	R2500I	GTC54-15A	2015-04-01	1.24	7	0.79–0.84
ULAS J122259.30+140750.1	J1222+1407	R300R	GTC8-15ITP	2016-01-19	1.04	6	1.16–1.34
DENIS J123218.3−095149	J1232−0951	R2500I	GTC54-15A	2015-05-31	1.32	23	2.06–2.19
2MASSW J1246467+402715	J1246+4027	R2500I	GTC54-15A	2015-04-29	1.05	2	0.63–0.67
2MASSW J1246467+402715	J1246+4027	R300R	GTC54-15A	2015-04-29	1.03	2	0.53–0.61
2MASS J13313310+3407583	J1331+3407	R2500I	GTC54-15A	2015-04-28	1.03	2	0.80–0.85
2MASS J13313310+3407583	J1331+3407	R300R	GTC54-15A	2015-04-28	1.01	2	0.79–0.91
2MASS J13334540−0215599	J1333−0215	R2500I	GTC8-15ITP	2015-12-31	1.23	7	1.28–1.36
2MASS J13460746+0842346	J1346+0842	R2500I	GTC8-15ITP	2016-01-06	1.09	6	1.01–1.07
2MASSW J1412244+163312	J1412+1633	R2500I	GTC8-15ITP	2016-01-19	1.06	6	1.26–1.34
2MASSW J1412244+163312	J1412+1633	R2500I	GTC54-15A	2015-04-29	1.04	2	0.62–0.66
2MASSW J1412244+163312	J1412+1633	R300R	GTC54-15A	2015-04-29	1.03	2	0.62–0.72
2MASSW J1421314+182740	J1421+1827	R2500I	GTC54-15A	2015-04-01	1.03	6	0.71–0.75
ULAS J143915.10+003941.7	J1439+0039	R300R	GTC8-15ITP	2016-03-29	1.16	10	0.57–0.66
DENIS J144137.2−094558	J1441−0945	R300R	GTC54-15A	2015-05-05	1.28	11	1.01–1.17
DENIS J144137.2−094558	J1441−0945	R2500I	GTC54-15A	2015-05-05	1.28	11	1.01–1.07
ULAS J152722.48+055316.2	J1527+0553	R300R	GTC8-15ITP	2016-03-29	1.15	11	0.76–0.88
2MASS J15322338+2611189	J1532+2611	R2500I	GTC8-15ITP	2016-01-29	1.08	17	0.82–0.87
2MASS J15394189−0520428	J1539−0520	R2500I	GTC8-15ITP	2016-02-27	1.46	44	1.42–1.51

Table A1 – *continued*

Object Full name	Object short name	Resolution Grism/ VPH	Programme ID	UT Date yyyy-mm-dd	Airmass (z)	Humidity (per cent)	Seeing $\lambda_{max} - \lambda_{min}$
2MASS J15485834−1636018	J1548−1636	R2500I	GTC54-15A	2015-04-01	1.47	10	1.10–1.17
2MASS J16170673+7734028	J1617+7733B	R2500I	GTC54-15A	2015-05-29	1.53	47	2.25–2.39
2MASS J16170673+7734028	J1617+7733B	R300R	GTC54-15A	2015-05-28	1.58	36	2.29–2.65
DENIS J161845.0−132129	J1618−1321	R2500I	GTC54-15A	2015-04-28	1.61	1	0.93–0.98
2MASS J16232185+1530393	J1623+1530	R2500I	GTC8-15ITP	2015-09-02	1.29	38	1.02–1.08
2MASS J16230740+2908281	J1623+2908	R2500I	GTC8-15ITP	2016-02-12	1.03	21	1.51–1.60
2MASS J17054834−0516462	J1705−0516	R300R	GTC54-15A	2015-04-01	1.21	7	1.08–1.24
2MASS J17072529−0138093	J1707−0138	R300R	GTC54-15A	2015-05-29	1.21	45	1.76–2.03
2MASS J17072529−0138093	J1707−0138	R2500I	GTC54-15A	2015-05-29	1.18	36	1.73–1.84
2MASS J17171408+6526221	J1717+6526	R2500I	GTC8-15ITP	2015-08-30	1.51	31	0.89–0.95
2MASS J17171408+6526221	J1717+6526	R300R	GTC54-15A	2015-05-03	1.42	4	0.75–0.87
2MASS J17171408+6526221	J1717+6526	R2500I	GTC54-15A	2015-06-01	1.27	39	2.01–2.14
Gaia DR2 4569300467950928768	J1724+2336	R300R	GTC8-15ITP	2015-09-01	2.13	28	1.36–1.58
DENIS J173342.3−165449	J1733−1654	R300R	GTC54-15A	2015-06-26	1.62	26	1.74–2.01
DENIS J174534.6−164053	J1745−1640	R2500I	GTC54-15A	2015-08-04	1.88	17	1.27–1.35
2MASS J17502484−0016151	J1750−0016	R2500I	GTC54-15A	2015-04-02	1.15	19	0.95–1.01
2MASS J21555848+2345307	J2155+2345	R2500I	GTC8-15ITP	2015-08-30	1.04	28	0.62–0.66
2MASS J23392527+3507165	J2339+3507	R2500I	GTC8-15ITP	2015-08-06	1.05	38	0.90–0.95

A2 Comparison with standard routines

In the reduction we use two procedures based on `IRAF` and `Python` packages with a comparison target (J1745−1640, DENIS J174534.6−164053; Phan-Bao et al. 2008) as a sanity check. A full image and spectral reduction was carried out using standard tasks within the `IRAF` package on one of our target objects (J1745–1640) plus complementary flux standard (Ross 640). This was done to assess both the quality of the data and to ascertain the necessary required reduction steps to maximize data quality. The results from this bespoke reduction method served as a reliable reference by which to measure the performance of a `python` pipeline (with support for the GTC/OSIRIS instrument recently added), which was later applied to all objects within our sample.

A2.1 Bespoke `IRAF` reduction

Our `IRAF` reduction was applied to the science and calibration frames of J1745−1640 (L1–1.5) and Ross 640 (DZA6) as appropriate using the following tasks, beginning with basic image reduction:

`CCDPROC` : Pre-scan bias level and bias structure removal; flat-fielding; illumination correction; data section trimming.

`RESPONSE` : Spectroscopic flat-field lamp colour removal (normalization).

`Illumination` and **`CCDPROC`**: Correction for spatial axis illumination gradients, made from the extensive sky lines of a well exposed object frame.

`IDENTIFY`, **`FITCOORDS`**, and **`TRANSFORM`**: Correction for geometric image distortion (curvature) along the spatial axis sky background.

For the spectral reduction:

`APALL` : Trace and extraction using both optimal and fixed-width aperture summing using image distortion corrected arc frames.

`IDENTIFY` and **`DISPCOR`**: Wavelength calibration to a linear wavelength dispersion using image distortion corrected arc frames.

`STANDARD`, **`SENSFUNC`**, and **`CALIBRATE`**: Flux calibration from the flux standard Ross 640 taken on same night as the target.

In addition to the `IRAF` tasks mentioned above, two extra reduction software tools were utilized during the reduction process:

`DeFringFlat` : An `IDL` routine aquired from the NASA `IDL` Astronomy library (Landsman 1993) was used to provide capabilities in de-fringing the flat field frames (DeFringFlat.pro; Rojo & Harrington 2006).

`SKYCALC` : ESO Sky Model Calculator provides additional telluric correction during flux calibration. A telluric sky model was queried using meteorological (e.g. moon phase, precipitable water vapour) and astrometric parameters (e.g. altitude, angular separation) appropriate for the object in question.

During the bias subtraction we discovered that the pre-scan region of the second CCD containing the spectrum displayed a gradient across it in ADU. A carefully chosen restricted section of the pre-scan region was used (∼3 pixels wide), which was found to be reliable for row-by-row bias level subtraction, before the 2D image bias structure was removed.

To correct for illumination gradients evident along the spatial axis of the 2D image introduced by the slit illumination function, we utilized the extensive sky lines of the well exposed object frames as a pseudo twilight sky flat (no sky flats were available). The `IRAFIllumination` task provided this functionality for correction, and we estimate that, after the correction was applied, the error introduced by the slit illumination gradient was reduced to a maximum of ∼1.5 per cent in the flat-field frames.

The latter, longer wavelength half of the flat-field frames showed evidence of fringing between wavelengths of approximately 8500 Å to 10 000 Å, coincident with the area of the CCD containing the spectra of interest. We used the `IDL` routine `DeFringFlat` as mentioned above to attempt to remove as much of the fringing as possible and found the best fit using the Morlet 'wavemother' model, and near default parameters. We estimate from measuring the cleaned flat-fielded image that the amplitude of the fringing was reduced from an original level of approximately 7 per cent, to a maximum of about 1.7 per cent.

A combined arc frame was made from the three arcs available from the night of observation to cover the entire wavelength region of the

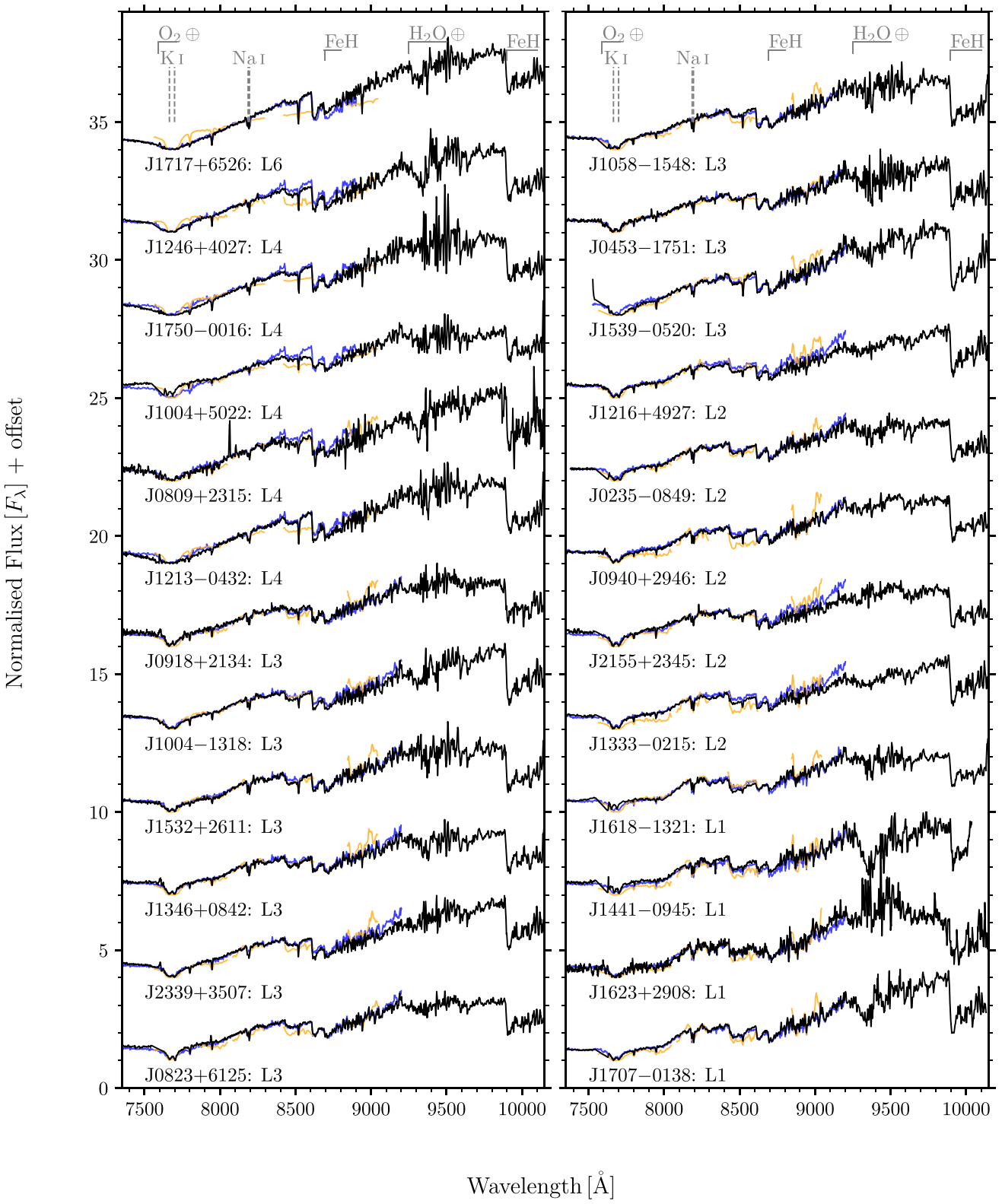

Figure A1. Same as Fig. 2 with additional comparison spectra. Light blue shows the corresponding standard optical spectra whilst light orange is the best-fitting BT-Settl model around the relevant spectral lines.

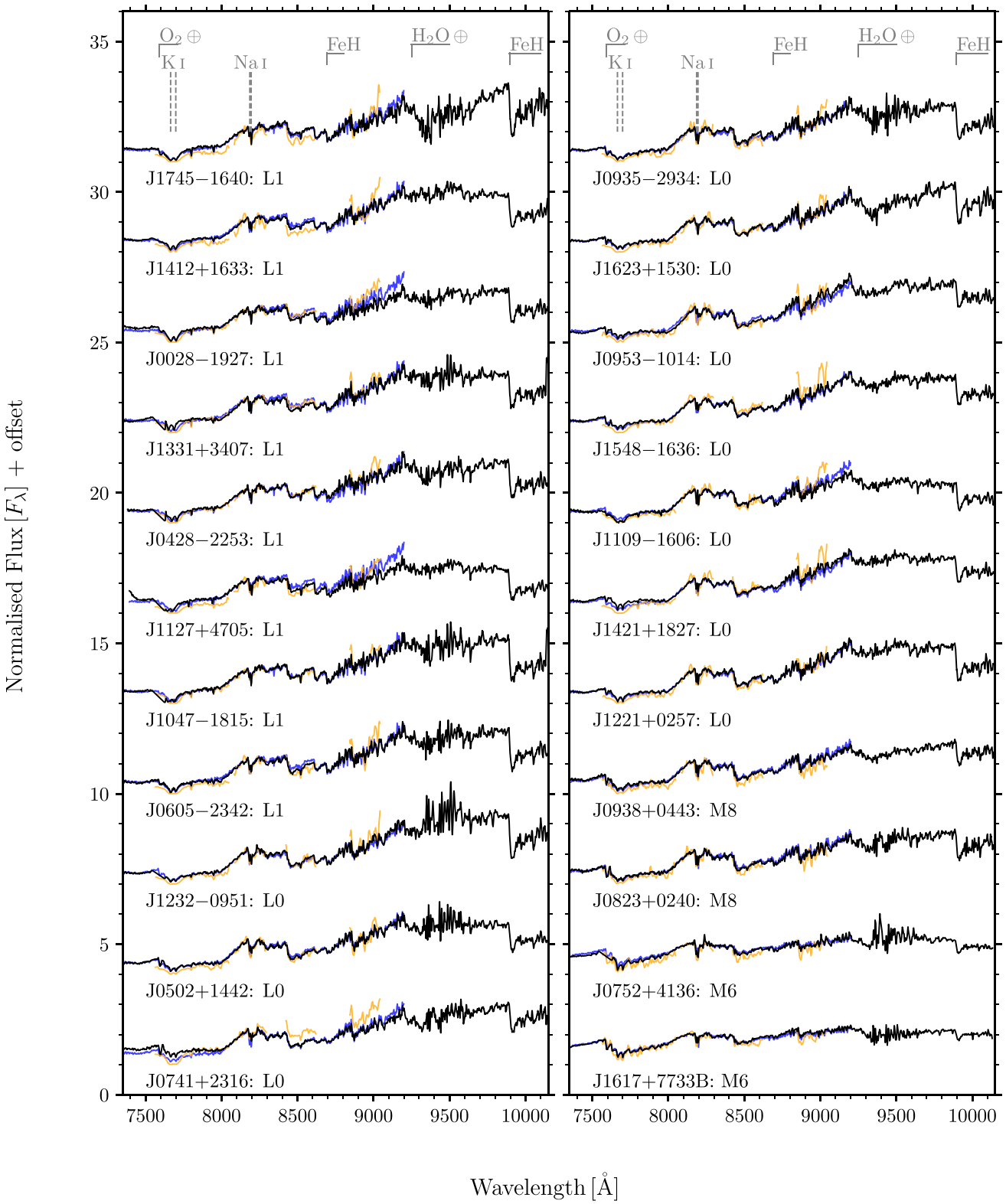

Figure A2. Same as Fig. A1 but for the second half of the R2500I VPHG spectral sample.

Table A2. Cross-matched absolute photometry from *Gaia*, 2MASS, and *WISE*, using *Gaia* parallaxes.

Object short name	M_G [mag]	M_{RP} [mag]	M_J [mag]	M_H [mag]	M_{K_s} [mag]	M_{W1} [mag]	M_{W2} [mag]	M_{W3} [mag]
J0028−1927	16.03 ± 0.02	14.45 ± 0.03	11.24 ± 0.04	10.38 ± 0.04	9.90 ± 0.04	9.57 ± 0.03	9.31 ± 0.03	8.88 ± 0.27
J0235−0849	17.04 ± 0.09	15.43 ± 0.10	12.26 ± 0.11	11.50 ± 0.11	10.88 ± 0.11	10.47 ± 0.10	10.19 ± 0.10	...
J0428−2253	16.70 ± 0.02	14.79 ± 0.02	11.48 ± 0.03	10.65 ± 0.03	10.10 ± 0.03	9.70 ± 0.03	9.45 ± 0.03	8.93 ± 0.13
J0453−1751	17.73 ± 0.04	16.15 ± 0.04	12.74 ± 0.05	11.66 ± 0.05	11.06 ± 0.05	10.55 ± 0.04	10.20 ± 0.04	9.62 ± 0.21
J0502+1442	15.59 ± 0.03	14.01 ± 0.04	10.96 ± 0.04	10.08 ± 0.04	9.64 ± 0.04	9.34 ± 0.05	9.10 ± 0.04	7.91 ± 0.22
J0605−2342	16.71 ± 0.02	15.16 ± 0.02	11.91 ± 0.04	11.13 ± 0.04	10.54 ± 0.04	10.24 ± 0.03	9.94 ± 0.03	10.05 ± 0.49
J0741+2316	16.40 ± 0.30	14.87 ± 0.32	11.73 ± 0.31	10.75 ± 0.31	10.34 ± 0.31	9.74 ± 0.30	9.43 ± 0.31	>7.16
J0752+4136	13.06 ± 0.03	11.59 ± 0.03	9.35 ± 0.04	8.79 ± 0.04	8.44 ± 0.04	10.36 ± 0.06	10.13 ± 0.09	>7.64
J0823+6125	17.65 ± 0.02	16.09 ± 0.03	12.80 ± 0.04	11.80 ± 0.04	11.18 ± 0.04	10.72 ± 0.03	10.43 ± 0.03	10.39 ± 0.39
J0847−1532	17.18 ± 0.01	15.60 ± 0.01	12.31 ± 0.03	11.43 ± 0.03	10.86 ± 0.02	10.51 ± 0.03	10.26 ± 0.02	9.76 ± 0.11
J0935−2934	16.39 ± 0.02	14.57 ± 0.03	11.42 ± 0.04	10.70 ± 0.04	10.21 ± 0.04	9.80 ± 0.03	9.51 ± 0.03	9.08 ± 0.21
J0938+0443	15.84 ± 0.07	14.31 ± 0.08	11.19 ± 0.09	10.44 ± 0.09	9.95 ± 0.10	9.75 ± 0.08	9.55 ± 0.08	>7.90
J0940+2946	16.57 ± 0.11	14.93 ± 0.12	11.56 ± 0.13	10.61 ± 0.13	10.19 ± 0.12	9.78 ± 0.11	9.52 ± 0.12	>8.78
J0953−1014	15.68 ± 0.02	14.03 ± 0.02	10.71 ± 0.03	9.88 ± 0.03	9.38 ± 0.03	9.01 ± 0.03	8.65 ± 0.03	7.97 ± 0.12
J1004+5022	18.45 ± 0.03	16.86 ± 0.03	13.15 ± 0.05	11.97 ± 0.05	11.10 ± 0.04	10.02 ± 0.03	9.46 ± 0.04	8.60 ± 0.07
J1004−1318	17.87 ± 0.03	16.29 ± 0.04	12.72 ± 0.05	11.92 ± 0.05	11.39 ± 0.05	10.82 ± 0.04	10.53 ± 0.04	10.21 ± 0.43
J1047−1815	16.76 ± 0.02	15.24 ± 0.02	11.96 ± 0.04	11.18 ± 0.04	10.65 ± 0.04	10.34 ± 0.03	10.08 ± 0.03	10.05 ± 0.47
J1058−1548	17.95 ± 0.01	16.39 ± 0.02	12.86 ± 0.04	11.93 ± 0.03	11.24 ± 0.03	10.79 ± 0.03	10.49 ± 0.03	10.40 ± 0.27
J1109−1606	16.56 ± 0.04	15.01 ± 0.05	11.89 ± 0.06	11.26 ± 0.06	10.81 ± 0.07	10.56 ± 0.05	10.26 ± 0.05	9.57 ± 0.48
J1127+4705	16.82 ± 0.05	15.23 ± 0.05	12.08 ± 0.06	11.38 ± 0.06	10.79 ± 0.06	10.49 ± 0.05	10.21 ± 0.06	9.57 ± 0.50
J1213−0432	18.71 ± 0.02	17.15 ± 0.03	13.54 ± 0.04	12.51 ± 0.03	11.87 ± 0.04	11.23 ± 0.03	10.93 ± 0.03	9.91 ± 0.22
J1221+0257	16.52 ± 0.01	14.93 ± 0.01	11.82 ± 0.02	11.06 ± 0.03	10.61 ± 0.03	10.30 ± 0.02	10.02 ± 0.02	9.48 ± 0.15
J1232−0951	16.43 ± 0.28	14.59 ± 0.28	11.42 ± 0.28	10.76 ± 0.28	10.24 ± 0.28	9.92 ± 0.28	9.64 ± 0.28	9.34 ± 0.39
J1246+4027	18.53 ± 0.03	16.95 ± 0.04	13.34 ± 0.06	12.20 ± 0.05	11.53 ± 0.05	10.83 ± 0.04	10.46 ± 0.04	10.21 ± 0.25
J1331+3407	16.72 ± 0.02	15.14 ± 0.02	12.04 ± 0.03	11.11 ± 0.04	10.59 ± 0.03	10.28 ± 0.03	10.05 ± 0.03	9.46 ± 0.23
J1333−0215	17.23 ± 0.07	15.60 ± 0.08	12.50 ± 0.08	11.49 ± 0.08	10.98 ± 0.09	10.66 ± 0.08	10.39 ± 0.08	9.69 ± 0.45
J1346+0842	17.32 ± 0.10	15.78 ± 0.11	12.58 ± 0.13	11.63 ± 0.13	11.00 ± 0.12	10.61 ± 0.11	10.38 ± 0.11	>9.08
J1412+1633	16.15 ± 0.02	14.55 ± 0.02	11.36 ± 0.03	10.63 ± 0.04	10.00 ± 0.03	9.66 ± 0.03	9.40 ± 0.03	8.89 ± 0.13
J1421+1827	16.45 ± 0.01	14.86 ± 0.01	11.85 ± 0.02	11.04 ± 0.02	10.56 ± 0.02	10.18 ± 0.02	9.91 ± 0.02	8.84 ± 0.05
J1441−0945	16.78 ± 0.09	14.86 ± 0.09	11.58 ± 0.09	10.75 ± 0.09	10.22 ± 0.09	9.90 ± 0.09	9.67 ± 0.09	9.67 ± 0.35
J1539−0520	17.85 ± 0.01	16.26 ± 0.02	12.79 ± 0.03	11.92 ± 0.03	11.44 ± 0.03	10.88 ± 0.03	10.61 ± 0.03	10.54 ± 0.28
J1548−1636	16.41 ± 0.02	14.87 ± 0.02	11.76 ± 0.03	10.98 ± 0.03	10.51 ± 0.03	10.16 ± 0.03	9.87 ± 0.03	9.35 ± 0.24
J1617+7733B	12.23 ± 0.01	10.87 ± 0.01	8.79 ± 0.02	8.21 ± 0.02	7.91 ± 0.02	7.62 ± 0.02	7.37 ± 0.02	7.13 ± 0.10
J1618−1321	16.04 ± 0.13	14.14 ± 0.13	10.95 ± 0.13	10.10 ± 0.13	9.62 ± 0.13	9.25 ± 0.13	8.99 ± 0.13	8.55 ± 0.36
J1623+1530	15.65 ± 0.20	14.10 ± 0.20	11.00 ± 0.22	10.20 ± 0.22	9.69 ± 0.22	9.53 ± 0.20	9.26 ± 0.21	7.53 ± 0.54
J1705−0516	16.81 ± 0.01	15.22 ± 0.01	11.94 ± 0.03	11.18 ± 0.03	10.66 ± 0.02	10.31 ± 0.03	10.05 ± 0.03	9.67 ± 0.21
J1707−0138	16.33 ± 0.03	14.72 ± 0.03	11.36 ± 0.04	10.64 ± 0.04	10.14 ± 0.05	9.71 ± 0.04	9.43 ± 0.04	9.32 ± 0.49
J1717+6526	18.56 ± 0.03	16.90 ± 0.03	13.25 ± 0.05	12.14 ± 0.04	11.48 ± 0.04	10.85 ± 0.03	10.52 ± 0.03	9.82 ± 0.07
J1724+2336	16.02 ± 0.07	14.45 ± 0.07	11.50 ± 0.09	10.95 ± 0.11	10.15 ± 0.11	10.03 ± 0.08	9.76 ± 0.08	>7.98
J1733−1654	17.20 ± 0.01	15.46 ± 0.01	12.23 ± 0.05	11.50 ± 0.06	11.05 ± 0.03	...	...	...
J1745−1640	16.98 ± 0.01	15.38 ± 0.01	12.18 ± 0.03	11.41 ± 0.02	10.94 ± 0.02	10.64 ± 0.03	10.40 ± 0.03	10.82 ± 0.46
J1750−0016	>18.47	16.86 ± 0.01	13.47 ± 0.02	12.59 ± 0.02	12.03 ± 0.02	11.36 ± 0.02	11.08 ± 0.02	10.47 ± 0.07
J2339+3507	18.26 ± 0.05	16.74 ± 0.06	13.16 ± 0.07	12.15 ± 0.07	11.38 ± 0.06	10.88 ± 0.05	10.56 ± 0.05	10.32 ± 0.53

spectrum. An initial wavelength solution was created and applied as part of the geometric image distortion correction, which resulted in a wavelength solution with an RMS error of 0.016 Å. A second wavelength calibration was subsequently made after additional reduction steps to ensure no systematic errors had been introduced, resulting in a more reasonable final RMS to the fitted wavelength solution of 0.025 Å. The final wavelength corrected spectrum had a linear dispersion 1.396 Å pixel^{-1} over the entire extracted range of 7339–10 155 Å.

Two separate flux calibrations were then made: one used a blackbody to represent the DZ white dwarf flux standard with an effective temperature 8070 K (Blouin, Dufour & Allard 2018) and with an *I*-band magnitude of 13.66 mag (Bergeron, Leggett & Ruiz 2001); the second used the low resolution calibrated flux standard spectrum of Ross 640 contained in the `IRAF` data base. In both cases, the sensitivity functions were created by interpolating over the affected telluric regions, and regions of intrinsic absorption features. Both of these sensitivity functions provided flux calibrations with almost identical results. A correction for atmospheric extinction and telluric features to the target was included during the flux calibration. An initial extinction correction was made from using a file containing tabulated extinction magnitudes as a function of wavelength applicable to the observatory site, that was provided on the GTC instrument website. However, an improved extinction correction was obtained from the much higher spectral resolution telluric sky model mentioned above (via the ESO Sky Model Calculator). The improvement is particularly evident over the wavelength regions containing the potassium K ιλλ7665,7699 Å doublet and the H_2O band at about 9500 Å.

A3 Radial velocity method validation

In keeping with our strategy outlined in Section A2 we again invoked an independent check, this time to validate our methods by helping to identify any problems with our RV measurements relating to the PYPEIT reduced data set. The techniques used to measure RVs via the centres of atomic neutral alkali lines and through cross-correlation of spectra were employed by Burgasser et al. (2015), and we adopt a similar twin measurement approach to derive our final RVs. We achieved this through the use of both IRAF and custom prepared routines within IDL to measure the RV via the Fourier cross-correlation and the line centre fitting methods. This analysis was conducted on the bespoke IRAF reduced data of our test object J1745−1640. We then used our validated RVs to classify any objects into young moving groups and stellar associations.

A3.1 Line centres

Two interactive methods were employed here: the first using routines in IDL to measure the 1D centroids of fitted Gaussian profiles to the atomic lines of J1745−1640, while the second used the IRAF task SPLOT to again measure the same lines but via fitting Voigt profiles.

In the first case, sub-sections of the spectrum surrounding the line features to be measured were extracted and interpolated onto a ten times finer wavelength grid, to facilitate the manual fitting of Gaussian profiles with a different number of terms via the GAUSSFIT.PRO routine. Best-fitting model profiles to spectral features were initially determined by eye, and determined by how closely the profile matched the feature with more emphasis being given around the line centre region. The reported RMS error and FWHM of fitted profiles were also taken into account for when the different Gaussian profiles produced similar results, such that the number of terms which fitted with the least error and narrowest FWHM were chosen. The measured wavelength shifts from laboratory rest-frame line centres (in standard air: Kramida et al. 2021) were then converted to Doppler RVs.

Secondly, and by using SPLOT, Voigt profiles were fitted to the same line features of appropriately pseudo-continuum subtracted subsections of the spectrum, and Doppler RVs were then found in the same manner as previously from the reported line centres. We obtained results for all eight line features from both measurement sets. However, it was apparent that four of the measurements gave the least error and particularly consistent results between both sets, these being Rb I-a, Rb I-b, Na I-a, Cs I-a with mean values for RV found from these four selected for each measurement set. The RV derived from the Gaussian fitted profiles (IDL) was found to be 35.1 km s^{-1}, and via Voigt profiles (SPLOT) 29.0 km s^{-1} (all test results are Heliocentric: barycentric correction calculated using BARYVEL.PRO). Typically, we found that Gaussian profiles were more reliable to fit but Voigt profiles were best for lines which could be successfully fit. From the spread among the individually measured line shifts we place more confidence in the latter result, and assign uncertainties based on the 1-σ standard deviation of the respective RV measurements of 4.3 and 3.8 km s^{-1}.

The RV as measured by our line centring method using the PYPEIT reduced data for J1745−1640 is 36.2 ± 4.4 km s^{-1} (see Table 4) which is in broad agreement with those from this independent measurement test. The RV measured via line centre fitting as reported by Burgasser et al. (2015) is 28 ± 9 km s^{-1}. Thus, we have confidence in our RV results derived from our chosen method, which contribute to the final adopted values.

A3.2 Cross-correlation

To validate this second technique of measuring RVs as part of our adopted method, and to ascertain the best way forward in its application, we used the Fourier cross-correlation task FXCOR within IRAF to conduct tests. Our choice of RV rest-frame models were a BT-Settl model spectrum and custom-made synthetic atomic absorption spectra. Our object was again the bespoke IRAF reduced J1745−1640 spectrum.

The BT-Settl spectrum used was the best-fitting model with the physical parameters of $T_{\rm eff} = 2000$ K, $\log g = 5$ dex, and Fe/H= 0 dex, corresponding to ≃L1 in spectral type. We smooth the spectrum using a Gaussian kernel to match the dispersion and resolution of the J1745−1640, and appropriate FITS header keywords added for the FXCOR task to recognize the template spectrum as rest-frame.

To help highlight any potential systematic wavelength shifts introduced by the use of the BT-Settl model, and therefore to help assess its suitability as an RV template, we measured the line centre locations of the most reliable Rb I-b and Cs I-a lines by fitting Voigt profiles in SPLOT. BT-Settl is known to generate models using a different line list to those selected in this work, where we used the NIST data base. A maximum difference compared to laboratory rest-frame line centres of 0.13 Å was found, corresponding to 4.5 km s^{-1}. This shift is similar to the uncertainty found earlier from the fitted line profiles suggesting that the BT-Settl model is reliable for use as a template, however, we add this uncertainty in velocity units in quadrature to the subsequent FXCOR individual RV region measurements.

To facilitate the most accurate RV measurements we extracted sections of both object and template spectra into discrete spectral regions, each covering the main atomic absorption features as well as the FeH Wing-Ford band at ∼9900 Å, then each region was appropriately pseudo-continuum subtracted and normalized.

During the RV measurements, we interactively adjusted the sample test wavelength range around the features of interest to reduce noise in Fourier space domain. Next, the width of the cross-correlation function (CCF) fit was changed to facilitate a best-fit (Gaussian fit to the CCF was used). The results of these changes to the CCF height, the goodness-of-fit '*R*-value' and fit error were noted, until the best RV estimate was obtained. The shape of the CCF profile was also informative to this end, it tended to be broad, with no apparent double peaks seen. No Fourier filtering was applied as it was not found to be beneficial.

For this test, three regions gave consistent results covering both of the rubidium lines, the first caesium line (≈ 8500 Å) and the FeH Wing-Ford band. The average of these individual results gave an RV of 21.2 ± 5.2 km s^{-1}.

For our second test, we created a noise-free synthetic absorption spectrum of unity continuum with line widths and depths as measured by Voigt profiles of the neutral atomic lines in of J1745−1640, with no attempt to include the FeH band. The line centres were fixed to the laboratory rest-frame wavelength values. Results from all four regions were averaged which covered both of the rubidium lines, the sodium doublet and both caesium lines. Including the potassium doublet gave a similar result for that region but gave a very large increase in uncertainty, so was not included. We find a resulting RV of 24.6 ± 1.7 km s^{-1}.

Our final test was conducted to ascertain the intrinsic level of uncertainty in RV from the application of this method through the use of FXCOR on a representation of our spectral data. This involved making a cross-correlation between two noise-free synthetic absorption spectra: the same RV rest-frame template as used above

in the second test, and with the object being a wavelength shifted version of the same synthetic spectrum, with the FITS header updated accordingly. The shift in wavelength was set at a value corresponding to the adopted RV presented in Burgasser et al. (2015), of $26.2 \pm 2.3\,\mathrm{km\,s^{-1}}$. We found the average combined RV of the four measured regions used to be $26.7 \pm 1.2\,\mathrm{km\,s^{-1}}$, indicating that $1.2\,\mathrm{km\,s^{-1}}$ is our base level uncertainty in using this method. This is, however, in addition to any uncertainty introduced from a real object spectrum (i.e. J1745−1640).

Both of these cross-correlation RV test results for J1745−1640 are in agreement with the equivalent value presented in Burgasser et al. (2015), within their respective uncertainties. The measured RV for J1745−1640 using the cross-correlation package we adopted and apply to our data set (see Section Section 4.3) has a value of $28.8 \pm 4.7\,\mathrm{km\,s^{-1}}$. Again, the results of this cross-correlation test validate our method and provide us with confidence in the separately derived RVs as well as in our final adopted values combined from both methods (see Section 4.3.3).

A4 Radial velocity measurement confidence

We demonstrate here a worked example for our test object, J1745−1640, including measurement uncertainties and our confidence metric. J1745−1640 had a wavelength calibration RMS of 0.077 Å. The wavelength shifts and uncertainties excluding this wavelength calibration RMS, i.e. the uncertainty corresponding to the fitted profile centre from the square root of the diagonal of the covariance matrix, are: K I-a 0.767 ± 0.397 Å; K I-b 0.713 ± 0.190 Å; Rb I-a 0.916 ± 0.112 Å; Rb I-b 0.542 ± 0.168 Å; Na I-a 0.537 ± 0.114 Å; Na I-b 1.237 ± 0.088 Å; Cs I-a 1.363 ± 0.051 Å; Cs I-b 0.330 ± 0.264 Å. We had experimented with several different metrics such as χ^2 but found that the root mean square deviation divided by the interquartile range (RMSDIQR) gave the most robust metric, especially when comparing across the two distinct techniques; those values were logged as follows. J1745−1640, Line Centring:

K I-a – Gaussian Profile with 17.4 Åσ; $30.0 \pm 18.5\,\mathrm{km\,s^{-1}}$; RMSDIQR=0.74. K I-b – Gaussian Profile with 12.2 Åσ; $27.8 \pm 10.4\,\mathrm{km\,s^{-1}}$; RMSDIQR=0.16. Rb I-a – Gaussian Profile with 2.1 Åσ; $35.2 \pm 7.2\,\mathrm{km\,s^{-1}}$; RMSDIQR=0.09. Rb I-b – Gaussian Profile with 2.2 Åσ; $20.4 \pm 9.2\,\mathrm{km\,s^{-1}}$; RMSDIQR=0.16. Na I-a – Voigt Profile with 2.4 Åσ; $19.7 \pm 7.0\,\mathrm{km\,s^{-1}}$; RMSDIQR=0.08. Na I-b – Voigt Profile with 2.8 Åσ; $45.2 \pm 6.0\,\mathrm{km\,s^{-1}}$; RMSDIQR=0.06. Cs I-a – Voigt Profile with 2.3 Åσ; $47.9 \pm 4.5\,\mathrm{km\,s^{-1}}$; RMSDIQR=0.04. Cs I-b – Gaussian Profile with 2.0 Åσ; $11.1 \pm 11.4\,\mathrm{km\,s^{-1}}$; RMSDIQR=0.25. RV Line Centre $=36.2 \pm 4.4\,\mathrm{km\,s^{-1}}$. J1745−1640, Cross Correlation:

K I-a – 2200 K, $\log g = 5.0$ dex; $30.0 \pm 5.0\,\mathrm{km\,s^{-1}}$; RMSDIQR=0.48. K I-b – 2200 K, $\log g = 5.0$ dex; $20.0 \pm 5.0\,\mathrm{km\,s^{-1}}$; RMSDIQR=0.20. Rb I-a – 2200 K, $\log g = 5.0$ dex; $35.0 \pm 5.0\,\mathrm{km\,s^{-1}}$; RMSDIQR=0.47. Rb I-b – 2000 K, $\log g = 5.0$ dex; $25.0 \pm 5.0\,\mathrm{km\,s^{-1}}$; RMSDIQR=1.25. Na I-a – 2100 K, $\log g = 5.0$ dex; $25.0 \pm 5.0\,\mathrm{km\,s^{-1}}$; RMSDIQR=1.33. Na I-b – 2000 K, $\log g = 5.0$ dex; $35.0 \pm 5.0\,\mathrm{km\,s^{-1}}$; RMSDIQR=0.79. Cs I-a – 2000 K, $\log g = 5.0$ dex; $55.0 \pm 5.0\,\mathrm{km\,s^{-1}}$; RMSDIQR=0.76. Cs I-b – 2000 K, $\log g = 5.0$ dex; $5.0 \pm 5.0\,\mathrm{km\,s^{-1}}$; RMSDIQR=0.89.

RV Cross Correlation $=28.8 \pm 4.7\,\mathrm{km\,s^{-1}}$. Adopted RV $=32.7 \pm 10.1\,\mathrm{km\,s^{-1}}$.

A5 Spectral sequence

We compare here in Figs A1 and A2 the sequence of R2500I spectra, as in Figs 2 and 3, to their appropriate standards and best-fitting BT-Settl models. All spectra are normalized by the median flux from 8100–8200 Å. The standards and BT-Settl models have been interpolated onto the wavelength grid of the spectra from this work. BT-Settl models have been additionally smoothed by a 2σ Gaussian kernel, so as to not 'dominate' the plot. These models are only plotted within ±100 Å of each spectral line listed in Table 2.

A6 `PYPEIT` Configuration files

A6.1 Reduction

```
slitspatnum  =  2:240
  [calibrations]
      [[biasframe]]
          exprng  =  None, 1
          [[[process]]]
              apply_gain  =  False
              combine  =  median
              use_biasimage  =  False
              use_overscan  =  False
              use_pixelflat  =  False
              use_illumflat  =  False
      [[darkframe]]
          exprng  =  999999, None
          [[[process]]]
              apply_gain  =  False
              use_biasimage  =  False
              use_overscan  =  False
              use_pixelflat  =  False
              use_illumflat  =  False
      [[arcframe]]
          [[[process]]]
              clip  =  False
              comb_sigrej  =  None
              use_overscan  =  False
              use_pixelflat  =  False
              use_illumflat  =  False
      [[tiltframe]]
          [[[process]]]
              comb_sigrej  =  None
              use_overscan  =  False
              use_pixelflat  =  False
              use_illumflat  =  False
      [[pixelflatframe]]
          [[[process]]]
              combine  =  median
              satpix  =  nothing
              use_overscan  =  False
              use_pixelflat  =  False
              use_illumflat  =  False
      [[pinholeframe]]
          exprng  =  999999, None
          [[[process]]]
              use_overscan  =  False
      [[alignframe]]
          [[[process]]]
              satpix  =  nothing
```

```
            comb_sigrej  =  None
            use_overscan  =  False
            use_pixelflat  =  False
            use_illumflat  =  False
    [[traceframe]]
        [[[process]]]
            use_overscan  =  False
            use_pixelflat  =  False
            use_illumflat  =  False
    [[illumflatframe]]
        [[[process]]]
            satpix  =  nothing
            use_overscan  =  False
            use_pixelflat  =  False
            use_illumflat  =  False
    [[skyframe]]
        [[[process]]]
            mask_cr  =  True
            use_overscan  =  False
    [[standardframe]]
        exprng  =  None, 600
        [[[process]]]
            combine  =  median
            spat_flexure_correct  =  True
            mask_cr  =  True
            use_overscan  =  False
    [[wavelengths]]
        reid_arxiv  =
        method  =  full_template
        lamps  =  XeI,HgI,NeI,ArI
        fwhm_fromlines  =  True
        ech_fix_format  =  False
        n_first  =  5
        n_final  =  6
        match_toler  =  2.
    [[slitedges]]
        sync_predict  =  nearest
        bound_detector  =  True
[scienceframe]
    exprng  =  600, None
    [[process]]
        mask_cr  =  True
        use_overscan  =  False
 combine  =  median
 spat_flexure_correct  =  True
[reduce]
    [[findobj]]
        maxnumber  =  2
[flexure]
    spec_method  =  slitcen
```

A6.2 Sensitivity function

```
[sensfunc]
    algorithm  =  IR
    mask_abs_lines  =  True
    polyorder  =  5
    samp_fact  =  1.0
    extrap_blu  =  0.5
    extrap_red  =  0.5
    [[IR]]
        objmodel  =  poly
        polyorder  =  3
        delta_redshift  =  0.
        fit_wv_min_max  =  [7350, 7550, 7750,
              8000, 8350, 8900, 9850, 10150]
```

A6.3 Flux calibration

```
[fluxcalib]
   extinct_correct  =  False

  flux read
   ../Science/<spec1d-standard.fits> sens-
func.fits
   ../Science/<spec1d-object.fits> sens-
func.fits
  flux end
```

A6.4 Coadding

```
[coadd1d]
   coaddfile  =  ../Science/<standard.fits>

  coadd1d read
   ../Science/<spec1d-standard.fits>
     SPAT0240-SLIT0457-DET02
  coadd1d end
  [coadd1d]
    coaddfile  =  ../Science/<object.fits>

  coadd1d read
   ../Science/<spec1d-object.fits>
     SPAT0240-SLIT0457-DET02
  coadd1d end
```

A6.5 Telluric correction

```
[telluric]
   objmodel  =  poly
   polyorder  =  5
   fit_wv_min_max  =  7350, 7550, 7750,
         8000, 8350, 8900, 9850, 10150
   maxiter  =  1
   popsize  =  300
   pix_shift_bounds  =  -10., 10.
```

This paper has been typeset from a TEX/LATEX file prepared by the author.